Title: Mega El Niño instigated the end-Permian mass extinction

Authors: Yadong Sun[1, 2]*†, Alexander Farnsworth[3,4]†, Michael M. Joachimski[2], Paul B. Wignall[5], Leopold Krystyn[6], David P.G. Bond[7], Domenico C.G. Ravidà[8], Paul J. Valdes[3,4]

Affiliations:

[1] State Key Laboratory of Biogeology and Environmental Geology, China University of Geosciences (Wuhan), Wuhan 430074, P.R. China

[2] GeoZentrum Nordbayern, Universität Erlangen-Nürnberg, Schlossgarten 5, 91054 Erlangen, Germany

[3] School of Geographical Sciences, University of Bristol, Bristol BS81SS, UK

[4] State Key Laboratory of Tibetan Plateau Earth System, Environment and Resources, Institute of Tibetan Plateau Research, Chinese Academy of Sciences, Beijing 100101, China

[5] School of Earth and Environment, University of Leeds, Leeds LS2 9JT, UK

[6] Department of Palaeontology, University of Vienna, Althanstrasse 14, A-1090 Wien, Austria

[7] School of Environmental Sciences, University of Hull, Hull, HU6 7RX, UK

[8] Department of Applied Geology, Georg-August-Universität Göttingen, Göttingen, Germany

*corresponding author E-mail: yadong.sun@cug.edu.cn

†These authors contributed equally to this work

Abstract: The ultimate driver of the end-Permian mass extinction is a topic of significant debate. Here, we use a multi-proxy and paleoclimate modelling approach to establish a unifying theory elucidating the heightened susceptibility of the Pangean world to prolonged and intensified El Niño events leading to an extinction state. As atmospheric pCO_2 doubled from ~410 to ~860 ppm in the latest Permian, the meridional overturning circulation collapsed, the Hadley cell contracted and El Niños intensified. The resultant deforestation, reef demise and plankton crisis marked the start of a cascading environmental disaster: reduced carbon sequestration initiated positive feedback, producing a warmer hothouse and, consequently, stronger El Niños. The compounding effects of elevated climate variability and mean state warming led to catastrophic but diachronous terrestrial and marine losses.

One-Sentence Summary:
The compounding effect of extreme El Niños and mean state warming led to catastrophic end-Permian losses.

Main Text:

The ultimate kill mechanism for the end-Permian mass extinction is uncertain. Rapid warming induced by eruptions of the voluminous Siberian Traps is regarded to have played a key role (*1*). However, over 20 volcanism-driven hyperthermals punctuate Phanerozoic history (*2*) and only a few coincide with extinctions, with none of them approaching the ~90% global species loss of the end-Permian (*3*). This raises the question of why the end-Permian world responded so strongly to CO_2-degassing and challenges our understanding of Earth system tipping points.

There is a clear mismatch in kill mechanisms and timing between marine and terrestrial losses during the end-Permian mass extinction (Fig. 1C). Equatorial sea surface temperature (SST) rose rapidly from ~26 °C to ~34 °C (*4*), likely exceeding the thermal tolerance of many marine organisms, particularly primary producers that underpin the marine food chain (*5*). However, many marine losses occurred ~17 kyr before substantial climate warming, suggesting that other kill mechanisms were at play: ocean deoxygenation is widely favored (*6*). However, in a setting characterized by atmospheric pO_2 levels higher than today (*7*), the impact of ocean anoxia on land would have been minimal. Even more puzzling, terrestrial extinctions, despite being diachronous themselves, began even earlier than the marine losses (*8, 9*), long before the potent warming. The loss of peatland (*10, 11*) and the replacement of gymnosperm forests by shrub-dominated terrestrial ecosystems (*12*) preceded the marine crisis by tens or even hundreds of thousands of years (*8*). Various causes have been proposed for the terrestrial crisis, including metal poisoning (*13*), intense UV-B radiation following ozone depletion (*14*) and acid rain (*15*). None of these alone can fully explain the scale, spatial heterogeneity, or the asynchronous nature of the end-Permian crisis.

Scant attention has been devoted to short-term climate oscillations occurring over interannual and interdecadal timescales in deep time, embedded within the context of longer-term climate change. Such modes of variability routinely induce large short-term fluctuations in temperature and the hydrological cycle through changes in weather patterns (*16*). We test the global climate system response to extreme greenhouse gas forcing in the Permian-Triassic (P-T) setting using paleotemperature proxy data to reconstruct the equatorial zonal SST gradient across the Tethys ocean (Fig. 1). Using a systematic combined approach incorporating proxy data, Earth system modelling (HadCM3BL) and sedimentary observations on a global scale, we establish a robust model for critical atmosphere-ocean coupling during the end-Permian catastrophe and propose a kill mechanism. We show that short-term climate fluctuations, which occur on annual time scales today, can be amplified by extreme greenhouse gas forcing, leading to a cascade of catastrophic terrestrial and marine losses.

Diminishing SST gradients

Zonal (east-west) and meridional (equator to mid-latitude) SST gradients regulate ocean-atmosphere feedback through Walker and Hadley circulations, and thus control low latitude climates. In modern oceans, a zonal SST gradient along the equator is prominent because equatorial easterlies push warm surface water to the west along both sides of the equator, generating a western warm pool. The westward movement of surface water also results in higher sea levels and a deeper thermocline in the western Pacific (*17*). Upwelling compensates for the loss of the warm surface layer in the east, generating cold tongues and a west-to-east tilted thermocline across the equatorial Pacific Ocean.

The P-T transition saw a dramatic decrease in the equatorial zonal SST gradient. Our paleotemperature dataset (*18*) shows that the late Permian equatorial zonal SST gradient within the Tethys was more prominent than that of modern Pacific. SSTs from westerly Cimmerian sites [e.g. Iran (*19*) and Armenia (*20*)] were consistently and considerably warmer than those from South China (*4*) in the east until 252.0 Ma. This zonal SST gradient decreased from >7–10°C in the late Permian, weakening to ~1–4°C across the P-T boundary, and was generally <4°C through the Early Triassic (Fig. 1B). The transition from high to low zonal SST gradients occurred abruptly within the latest Permian *Clarkina yini* conodont Zone (Fig. 1C).

Although less pronounced, our model simulations replicate these proxy data changes and additionally show an expanded equatorial warm pool and substantial thermocline deepening (Figs. S1 to S3). These profound changes in the ocean's thermal structure had substantial consequences for atmospheric circulation. Walker circulation weakened with the rising and sinking limbs both contracting to Panthalassa (Fig. 2). These changes coincide precisely with the decrease in the equatorial zonal SST gradient (Fig. 1C), leading to reduced horizontal and vertical moist advection. The ascending limb of the tropical Hadley circulation, already weaker than in the modern era, weakened further with warming, contracting in terms of both tropical overturning and convective potential (Figs. S4 and S5). Simultaneously, the descending limb widens at 500 hPa in the mid-latitudes, expanding arid regions poleward—a key feature of P-T sedimentary records (Fig. S6) and a climatic response predicted in future warming scenarios (*21*).

El Niño in a hothouse world

As the zonal SST changes are both the cause and consequence of Walker circulation fluctuations (*22*), flattened zonal SST gradients and weakened Walker circulation collectively imply a high probability of El Niños. Our proxy data showing diminished zonal SST gradients are mainly derived from the Tethys Ocean with further information coming from Panthalassa. They alone do not permit evaluation of the impact of El Niño Southern Oscillation (ENSO) due to its fine temporal scale, but we can address this in our Earth system modelling using the oceanic Niño index and by defining the Niño 3.4 (5°N–5°S, 120°–170°W) as equivalent to Panthalassa (Fig. 1A). We test this definition using empirical orthogonal function (EOF) analysis, which shows a strong 57.1% variance in the equivalent to the Niño 3.4 region of the Pacific, suggesting that Panthalassa's configuration is broadly similar to the modern Pacific. A series of pCO_2 sensitivity tests is carried out to understand the impact of warming on ENSO variability and its role in driving extinctions.

Model simulations show that SST anomalies in the Niño 3.4 equivalent region increase in both amplitude and longevity as atmospheric pCO_2 increases from 412 to 4000 ppm. Thus, the SST positive anomalies, marking El Niño conditions, increase from ~0.5–1.5°C in the Changhsingian prior to the main eruptions of Siberian Traps to ~4°C during maximum warmth in the Induan (Early Triassic), whilst their periodicity increases from 2–5 to 7–9 years (Fig. S7). These increases were accompanied by a disappearance of the El Niño-La Nina amplitude and evolution asymmetry (Fig. 3).

The disappearance of eastern cold tongues is a typical feature of El Niño conditions, but it is generally challenging to verify this with ancient proxy data. However, our conodont $\delta^{18}O$ values from the upper Smithian in Idaho (16.9 ‰) are comparable to contemporary $\delta^{18}O$ values from South China (16.8 ‰), Croatia (16.7 ‰), and Italy (16.5 ‰). Thus, the $\delta^{18}O$ difference, close to analytical reproducibility (±0.14 ‰, 1 σ), suggests that the Panthalassan "cold tongue" areas were

as warm as Tethys. These $\delta^{18}O$ values are comparable to those from Oman (16.3 ‰, ~20–30°S), suggesting there was an enormous warm pool across low latitude oceans, with SSTs reaching 39.4–41.9°C, and this extended to the extratropics during the hottest time of the Early Triassic. The warm "cold tongue" was accompanied by the cessation of denitrification on the eastern Panthalassan margin (*23*). The high SSTs of the late Smithian require atmospheric pCO_2 that was much greater than 4000 ppm to drive. However, our model simulations already show a steady deepening of the thermocline from ~30 m to over ~100 m across the P-T transition in eastern Panthalassa (Fig. S3). Together with weakened Walker circulation, this led to a reduction in equatorial upwelling. Collectively, proxy and modelling evidence suggests that the mean state warming in both Tethys and Panthalassa at the P-T boundary was probably El Niño-like.

Homogeneous SSTs along the equator weaken easterlies (both mean state and during El Niños) by reducing the east-west near-surface pressure gradient—a consistent feature of El Niños in the modern. Such changes link to sea level fluctuations that are also observed across the Tethys and Panthalassa oceans in the P-T time (*24*). There is no known evidence for ice coverage during the P-T interval and glacio-eustatic changes were insignificant. We suggest that regression recorded in some Tethyan sections in the west while transgressions featured along the eastern Panthalassan margin [e.g., western USA (*24, 25*)] was a function of strong ENSO impacting sedimentary records.

Was mega El Niño a permanent El Niño?

Whether climate warming has a significant impact on the strength and duration of El Niño is a matter of topical debate. Modern El Niños occur intermittently every two to seven years and typically last nine to 12 months but may have persisted for ~3 Myr in the Pliocene (*26*). Many features of future El Niños simulated by CMIP6 models remain uncertain, but stronger El Niños with fast onset and slow decay will likely occur (*27*).

Our simulations suggest that as the world warmed across the P-T boundary both the magnitude and duration of El Niño increased but this was not accompanied by the establishment of a permanent El Niño (Fig. 3). Our proxy-derived zonal SST gradients across the equatorial Tethys show consistently high values in the Permian and consistently low values in the Early Triassic (Fig. 1, B and C). This should not be interpreted as an establishment of permanent El Niño but is a function of the time-averaged homogenization of paleotemperatures in "bulk" samples. Each data point was measured from ~50 conodonts from a sub-10–100 kyr interval thereby averaging any short-term anomaly. Our data collectively indicate that the Permian was largely dominated by neutral ENSO states, whilst El Niños became prominent shortly before the P-T boundary, to an extent that influenced the long-term climate proxy record in the Tethys (Fig. 1B), but did not diminish the simulated zonal SST anomalies in the Panthalassa (Fig. 3; *18*).

Climate States

The transition to conditions with prolonged, episodic mega-ENSO events created a world of exceptional climate variability (Fig. 3), with intra-annual variability controlled by the large land-ocean thermal contrast of Pangea (*28*), and annual to decadal variability controlled by ENSO, whilst millennial variability was controlled by pCO_2 and possibly orbital forcing. The net result was a broadly hot but extraordinarily unstable and variable climate (Fig. 4, and Figs. S8, S9, S11 to S14).

On land, low and mid-latitude climates became nearly unified across the P-T boundary, leading to a remarkable transition from regionally-diverse sedimentary facies to higher-energy fluvial sedimentation style, frequently represented by braided river facies assemblages (Fig. S6). This shift signals the onset of a more unstable climate state, characterized by moisture deficits and irregular rainfall, coupled with generally greater surface runoff and temperature extremes (*18*). Such conditions, presumably driven by both Pangean monsoon and ENSO cycles, occurred poleward and equatorward from ~10° to ~60° in both hemispheres but are less apparent in high-latitudes (*29*), probably because ENSO is primarily a low-latitude climate anomaly (Fig. 4; Fig. S9).

Unlike other hothouse intervals such as the middle Cretaceous (*30*), in the P-T case, the ascending limb of the Hadley cells weakened and contracted while the descending limb expanded further towards the poles (Figs. S4, S5). This is clearly manifested in the Turpan-Kumul Basin (Xinjiang, NW China), where plant-bearing Upper Permian fluvial-lacustrine and deltaic depositional systems are abruptly overlain by Lower Triassic drylands, suggesting a sudden shift in climate regime at ~44°N (Fig. S6A). These areas were probably as dry as modern subtropical deserts, but with pronounced seasonal torrential rains, indicated by the common occurrence of sheet-like sandstones and pebbly deposits produced by flash flooding and ephemeral rivers (Fig. S6, B to D). The transition to higher-energy fluvial systems across the P-T boundary has been previously attributed to reduced bank stability from plant die-off (*31*), but this also occurs in extremely arid settings where pre-crisis vegetation was already minimal or absent (*32*). We propose that the shift to a much more irregular precipitation regime was the main driver of the P-T sedimentary evolution on land.

Stronger El Niños and warmer hothouse

The decrease in the zonal SST gradient at the end of the Permian during an El Niño likely caused two inter-connected positive feedbacks through interplays with the Walker circulation. Weakened easterlies led to the eastward retreat of warm waters, deepening the thermocline in the east (Fig. S3), which in turn further enhanced El Niño conditions (Bjerknes feedback, *17, 22*). The development of increasingly stronger El Niños is simultaneously coupled with changes in the low latitude hydrological cycle. Warm waters generate high, rain-bearing convective clouds that are less reflective than low, non-rain-bearing stratus clouds that follow cooler waters. Thus, El Niño redistributes low latitude precipitation as the warm pool expands eastward (*33*). Decreases in low latitude coverage by stratus clouds would also reduce the overall planetary albedo, exacerbating hothouse conditions.

Impact on the terrestrial realm

The synergy of stronger ENSO and a warm climate generates an oscillating dry-wet contrast over land and amplifies the unevenness of precipitation on a global scale (Fig. 4). During El Niños, the heat stored in the ocean is released into the atmosphere, leading to severe drought and extreme heat. Today, these conditions have destabilized tropical forests, causing Amazonian and African rainforest dieback (*34, 35*). In the P-T time, our composite analysis of five consecutive ENSO intervals reveals large climate anomalies compared to the background state. These include a strong, high-temperature land-ocean teleconnection in the tropics and extratropics, mildly cooler high latitudes, and a re-distribution of low latitude precipitation predominantly over Panthalassa

and around the Tethys margins during El Niños (Fig. 4). Roughly opposite trends occur during La Ninas (Fig. S9). Geologic evidence for these changes includes the widespread development of fluvial facies produced by irregular runoff and flashy discharge in the Early Triassic (Figs. S6, S10), indicating an unprecedented homogeneity of low latitude climates that featured highly variable dry and wet seasons (Figs. S11to S14).

As the duration of El Niños extended from months to years (Fig. 3), prolonged warmth and drought in vast areas of Pangea would have stressed plants further amidst background warming and an increased frequency of wildfires. This is evidenced by the zenith of charcoal deposition in equatorial peatlands as the climate regime transitioned from humid to semi-arid (*11*). Wet periods created substantial fuel reserves and were followed by long-lasting droughts with accompanying heat that resulted in severe wildfires. This drove the eventual extinction of rainforest plants and, consecutively, the collapse of the charcoal "spike" (Fig. 1C), reflecting the loss of terrestrial biomass and fuel for fire. As warming and aridity intensified, vegetation was increasingly subject to fire susceptibility (Fig. S15), compromising carbon sequestration in the terrestrial realm (*10*) and elevating atmospheric pCO_2 further.

Frequent droughts force physiological changes in plants and favor short-lived taxa capable of thriving in sporadic wet intervals whilst enduring prolonged dry spells in their seed or spore stage. This is reflected by a floral shift in preference across the P-T crisis towards lightly-built shrubs rather than trees, as indicated by the post-extinction prevalence of the isoetalean lycopsids *Pleuromeia* and *Annalepis*, in contrast to the gymnosperm-dominated forests of the Permian (*36*). A similar adaptation to life cycles exploiting brief wet intervals probably explains the selective survival of insect groups. Their fossil record, although patchy, reveals significant declines in most groups, closely linked to the loss of habitats and food plants (*37*) during deforestation (Fig. S16). However, those with aquatic larval stages (e.g., amongst palaeopteran families) fared better than those with an entirely terrestrial life cycle (*37*), indicating an ability to exploit the wet intervals. Early Triassic assemblages were dominated by beetles, cockroaches and mayflies (*37, 38*). However, the post-extinction climatic conditions were overall harsh (Fig. S8; *39*), with none of the major insect groups showing opportunistic radiation (*37*).

The extreme effects of ENSO were most clearly manifest in low latitude ocean-atmosphere interactions, but their consequences were global (Fig. 4) and ensured that the modest changes in mean background conditions were greatly amplified (Fig. 5). The most prominent change in the P-T terrestrial realm was the dramatic deforestation in both hemispheres in response to the initial pCO_2 doubling. Our simulations indicate that the southern deciduous taiga was impacted first. It retreated poleward in Gondwana and decreased by 46.6% in coverage (equivalent to ~ 21×10^6 km^2 forest loss) within ~25 kyr (Fig. S16). This was followed by successive deforestation in northern mid-latitudes and tropics (Fig. S16), a pattern confirmed by the fossil record of the regions (*8, 9, 40*). However, what drove the earlier deforestation in southern high latitudes is unexplained. The disappearance of the Permian *Glossopteris* flora in the Sydney Basin (70°S) occurred ~380 kyr (*8*) before the rise in equatorial SSTs. Our simulations indicate the region was particularly vulnerable to ENSO impact, much like Australia today (Fig. 4 and Fig. S9). Specifically, warmer and dryer summers were prominent during El Niños (Fig. S14), aligning with sedimentological evidence for increasingly prolonged droughts at the level directly above the last Permian flora (*29*).

Impact on the marine realm

Most phytoplankton and zooplankton have a thermal tolerance up to ~35°C, but the optimal temperature range for vital processes (e.g. reproduction) is often narrower than the range required for survival (*5*), particularly in species with lifespans shorter than a year. Consequently, marine plankton are particularly susceptible to inter-annual climate perturbations. Their decline can trigger bottom-up trophic cascades, as seen during recent marine heat waves (*41*). The P-T transition witnessed a turnover in the composition of primary producers, whereby the dominant eukaryotic plankton groups became extinct and were replaced by bacteria (including cyanobacteria), acritarchs and prasinophytes (*42*). The changes amongst plankton groups are also faithfully documented by a crisis amongst radiolarians (*43*), a heterotrophic group with siliceous skeletons that have a good fossil record. They suffered major losses ~40 kyrs prior to the main marine losses, coincident with the onset of enhanced El Niños (Fig. 1C) indicating that planktonic communities were the first to be stressed by augmented interannual variability and climatic extremes (Fig. 1C).

Reefs are amongst the most vulnerable components of marine ecosystems. Both coral and non-coral reefs have suffered mass mortality in recent marine heat waves (*5*), underscoring their limited capacity to withstand rapid SST increases. The end-Permian crisis saw not only the extinction of all Paleozoic corals but the demise of metazoan reefs of all types (*44*), leading to one of the Phanerozoic's most prominent reef gaps (*45*). The last Permian reefs persisted to a level correlative with the top of Meishan stratotype Bed 23 (*44, 46*). Thus, their demise coincided with the advent of intensified El Niños and the weakening of global Meridional Ocean Circulation (MOC; Fig. 1C and Fig. S17), heralding the severe losses to come.

The main marine mass extinction coincides with the onset of widespread ocean anoxia and postdates the start of a major negative carbon isotope excursion (Fig. 1). Anoxia occurred during a phase of rapid ocean warming, increasing stratification and reorganization of the global MOC, which was likely a consequence of these changes (Figs. S1 to S3 and S17). The MOC collapsed from its robust pre-crisis state, featuring a strong, well-mixed cell with mid- and deepwater overturning in the northern hemisphere, to a shallower northward cell as pCO_2 doubled from 412 ppm to 857 ppm (Fig. S17). The proxy-recorded onset of ocean anoxia at Meishan (*47*) is attributed to a global expansion of anoxic water masses, and lagged the collapse of the MOC by ~3–5 kyr—a brief interval comparable to the residence time of seawater. The MOC mixing cells weakened and shallowed further with increasing pCO_2 (Fig. S17), suggesting the pre-crisis P-T world was already highly sensitive to small changes in pCO_2.

An El Niño-instigated extinction

The shift to a new climate state with enhanced variability at the end of the Permian was likely rapid. Employing a Bayesian age model grounded in U-Pb dating (*48*), the transition is estimated to have occurred within ~5 ± 3 kyr, predating the onset of marine extinction by ~40±30 kyr. This coincided with the onset of a protracted decrease in $\delta^{13}C$ and a minor, ~4°C increase in equatorial SST (Fig. 1C). Because Upper Permian marine faunas maintained their diversity, it is generally thought that there were no environmental perturbations at this time. However, two-thirds of the volume of Siberian Traps lava and pyroclastic eruptions occurred pre-extinction (*1*), and our study shows that they coincide with progressively enhanced ENSO activity (Figs. 1 and 3). The

initiation of a major crisis, encompassing deforestation on land (*8*), the collapse of MOC, extinctions in marine plankton, and the demise of reefs, all occurred during the initial pCO_2 doubling to 857 ppm and coincided with a decrease in the equatorial zonal SST gradient in Tethys (Fig. 1 and Figs. S16, S17). Thus, in the P-T world, even relatively small greenhouse gas emissions and warming were sufficient to tip the climate into a state characterized by prolonged and intense El Niño phases. This introduced extremes in low latitude temperature and precipitation that stressed terrestrial ecosystems (Figs. 4 and 5). Drought intervals were too prolonged for trees to survive, strongly favoring opportunists amongst both plants and insects that were able to complete their life cycle during wet periods. In the ocean, planktonic groups, with their sub-annual lifecycles, were also severely impacted, but the resilience of the marine biosphere ensured its survival until it succumbed to progressive warming and ocean de-oxygenation. The losses in biomass, in turn, reduced carbon sequestration, creating a warmer hothouse with stronger El Niños.

Conclusions

El Niño events today are known to cause coral bleaching (*5*), the mass mortality of fish and birds (*49*), and they have profound impacts on human society. However, the ecological impact and future trajectory of extreme El Niños against a backdrop of global warming is not yet known. The Pangean supercontinent paleogeography was seemingly more susceptible to ever-increasing ENSO events with increasing pCO_2. The end-Permian crisis reveals that intensified ENSO increases the risk of extinction, enhancing low latitude warmth that in turn created stronger El Niños. For terrestrial communities, prolonged extremes (droughts and high temperatures) led to extinctions, whilst the oceans suffered from heat stress and the expansion of anoxia, with equally disastrous consequences for life. Because the oceans warm more slowly than land and marine organisms have higher motility (actively or passively), terrestrial ecosystems are more vulnerable to extinction threats during intensified El Niños. Consequently, the P-T transition saw the marine extinction lag by ~40±30 thousand years, a short interval geologically, and one that is alarmingly, on human timescales, as we move towards an ever more variable climate regime.

References and Notes

1. S. D. Burgess, S. A. Bowring, High-precision geochronology confirms voluminous magmatism before, during, and after Earth's most severe extinction. *Science Advances* **1**, e1500470 (2015).
2. C. R. Scotese, H. Song, B. J. W. Mills, D. G. van der Meer, Phanerozoic paleotemperatures: The earth's changing climate during the last 540 million years. *Earth-Science Reviews* **215**, 103503 (2021).
3. J.-x. Fan *et al.*, A high-resolution summary of Cambrian to Early Triassic marine invertebrate biodiversity. *Science* **367**, 272-277 (2020).
4. M. M. Joachimski *et al.*, Climate warming in the latest Permian and the Permian-Triassic mass extinction. *Geology* **40**, 195-198 (2012).
5. K. E. Smith *et al.*, Biological Impacts of Marine Heatwaves. *Annual Review of Marine Science* **15**, 119-145 (2023).
6. P. B. Wignall, R. J. Twitchett, Oceanic Anoxia and the End Permian Mass Extinction. *Science* **272**, 1155-1158 (1996).

7. B. J. W. Mills, A. J. Krause, I. Jarvis, B. D. Cramer, Evolution of Atmospheric O2 Through the Phanerozoic, Revisited. *Annual Review of Earth and Planetary Sciences* **51**, 253-276 (2023).
8. C. R. Fielding *et al.*, Age and pattern of the southern high-latitude continental end-Permian extinction constrained by multiproxy analysis. *Nature Communications* **10**, 385 (2019).
9. R. A. Gastaldo *et al.*, The base of the Lystrosaurus Assemblage Zone, Karoo Basin, predates the end-Permian marine extinction. *Nature Communications* **11**, 1428 (2020).
10. G. J. Retallack, J. J. Veevers, R. Morante, Global coal gap between Permian-Triassic extinction and Middle Triassic recovery of peat-forming plants. *Geological Society of America Bulletin* **108**, 195-207 (1996).
11. D. Chu *et al.*, Ecological disturbance in tropical peatlands prior to marine Permian-Triassic mass extinction. *Geology*, (2020).
12. C. V. Looy, W. A. Brugman, D. L. Dilcher, H. Visscher, The delayed resurgence of equatorial forests after the Permian–Triassic ecologic crisis. *Proceedings of the National Academy of Sciences of the United States of America* **96**, 13857-13862 (1999).
13. D. Chu *et al.*, Metal-induced stress in survivor plants following the end-Permian collapse of land ecosystems. *Geology*, (2021).
14. F. Liu *et al.*, Dying in the Sun: Direct evidence for elevated UV-B radiation at the end-Permian mass extinction. *Science Advances* **9**, eabo6102 (2023).
15. B. A. Black, J.-F. Lamarque, C. A. Shields, L. T. Elkins-Tanton, J. T. Kiehl, Acid rain and ozone depletion from pulsed Siberian Traps magmatism. *Geology* **42**, 67-70 (2014).
16. M. R. Allen, W. J. Ingram, Constraints on future changes in climate and the hydrologic cycle. *Nature* **419**, 224-232 (2002).
17. M. Latif, N. S. Keenlyside, El Niño/Southern Oscillation response to global warming. *Proceedings of the National Academy of Sciences* **106**, 20578-20583 (2009).
18. See supplementary materials.
19. M. Schobben, M. M. Joachimski, D. Korn, L. Leda, C. Korte, Palaeotethys seawater temperature rise and an intensified hydrological cycle following the end-Permian mass extinction. *Gondwana Research* **26**, 675-683 (2014).
20. M. M. Joachimski, A. S. Alekseev, A. Grigoryan, Y. A. Gatovsky, Siberian Trap volcanism, global warming and the Permian-Triassic mass extinction: New insights from Armenian Permian-Triassic sections. *GSA Bulletin* **132**, 427-443 (2020).
21. B. I. Cook *et al.*, Twenty-first century drought projections in the CMIP6 forcing scenarios. *Earth's Future* **8**, e2019EF001461 (2020).
22. A. V. Fedorov, S. G. Philander, Is El Niño changing? *Science* **288**, 1997-2002 (2000).
23. S. D. Schoepfer, C. M. Henderson, G. H. Garrison, P. D. Ward, Cessation of a productive coastal upwelling system in the Panthalassic Ocean at the Permian–Triassic boundary. *Palaeogeography, Palaeoclimatology, Palaeoecology* **313-314**, 181-188 (2012).
24. P. B. Wignall, A. Hallam, Anoxia as a cause of the Permian/Triassic mass extinction: facies evidence from northern Italy and the western United States. *Palaeogeography, Palaeoclimatology, Palaeoecology* **93**, 21-46 (1992).
25. B. Kummel, Paleoecology of Lower Triassic formations of southeastern Idaho and adjacent areas. *Geological Society of America Memoirs* **67**, 437-468 (1957).
26. M. W. Wara, A. C. Ravelo, M. L. Delaney, Permanent El Niño-like conditions during the Pliocene warm period. *Science* **309**, 758-761 (2005).
27. H. Lopez, S.-K. Lee, D. Kim, A. T. Wittenberg, S.-W. Yeh, Projections of faster onset and slower decay of El Niño in the 21st century. *Nature Communications* **13**, 1915 (2022).

28. Y. Hu *et al.*, Emergence of the modern global monsoon from the Pangaea megamonsoon set by palaeogeography. *Nature Geoscience*, (2023).
29. C. R. Fielding *et al.*, Sedimentology of the continental end-Permian extinction event in the Sydney Basin, eastern Australia. *Sedimentology* **68**, 30-62 (2021).
30. H. Hasegawa *et al.*, Drastic shrinking of the Hadley circulation during the mid-Cretaceous Supergreenhouse. *Climate of the Past* **8**, 1323-1337 (2012).
31. P. D. Ward, D. R. Montgomery, R. Smith, Altered river morphology in South Africa related to the Permian-Triassic extinction. *Science* **289**, 1740-1743 (2000).
32. C. M. S. Scherer *et al.*, The stratigraphic puzzle of the permo-mesozoic southwestern Gondwana: The Paraná Basin record in geotectonic and palaeoclimatic context. *Earth-Science Reviews* **240**, 104397 (2023).
33. G. A. Vecchi, A. T. Wittenberg, El Niño and our future climate: where do we stand? *WIREs Climate Change* **1**, 260-270 (2010).
34. J. C. Jiménez-Muñoz *et al.*, Record-breaking warming and extreme drought in the Amazon rainforest during the course of El Niño 2015–2016. *Scientific Reports* **6**, 33130 (2016).
35. J.-P. Wigneron *et al.*, Tropical forests did not recover from the strong 2015–2016 El Niño event. *Science Advances* **6**, eaay4603 (2020).
36. S. F. Greb, W. A. DiMichele, R. A. Gastaldo, in *Wetlands Through Time. Geological Society of America Special Paper 399,* S. F. Greb, W. A. DiMichele, Eds. (Geological Society of America, Boulder, CO, 2006), pp. 1-40.
37. C. Jouault, A. Nel, V. Perrichot, F. Legendre, F. L. Condamine, Multiple drivers and lineage-specific insect extinctions during the Permo–Triassic. *Nature Communications* **13**, 7512 (2022).
38. D. E. Shcherbakov, Madygen, Triassic Lagerstätte number one, before and after Sharov. *Alavesia* **2**, 113-124 (2008).
39. Y. D. Sun *et al.*, Lethally hot temperatures during the Early Triassic greenhouse. *Science* **338**, 366-370 (2012).
40. W. Guo *et al.*, Late Permian–Middle Triassic magnetostratigraphy in North China and its implications for terrestrial-marine correlations. *Earth and Planetary Science Letters* **585**, 117519 (2022).
41. L. A. Arteaga, C. S. Rousseaux, Impact of Pacific Ocean heatwaves on phytoplankton community composition. *Communications Biology* **6**, 263 (2023).
42. C. Cao *et al.*, Biogeochemical evidence for euxinic oceans and ecological disturbance presaging the end-Permian mass extinction event. *Earth and Planetary Science Letters* **281**, 188-201 (2009).
43. Q. Feng *et al.*, Radiolarian evolution during the latest Permian in South China. *Global and Planetary Change* **55**, 177-192 (2007).
44. R. C. Martindale, W. J. Foster, F. Velledits, The survival, recovery, and diversification of metazoan reef ecosystems following the end-Permian mass extinction event. *Palaeogeography, Palaeoclimatology, Palaeoecology* **513**, 100-115 (2019).
45. W. Kiessling, Geologic and biologic controls on the evolution of reefs. *Annual Review of Ecology, Evolution, and Systematics* **40**, 173-192 (2009).
46. X. Li *et al.*, Factors controlling carbonate platform asymmetry: Preliminary results from the Great Bank of Guizhou, an isolated Permian–Triassic Platform in the Nanpanjiang Basin, south China. *Palaeogeography, Palaeoclimatology, Palaeoecology* **315-316**, 158-171 (2012).
47. L. Xiang *et al.*, Oceanic redox evolution around the end-Permian mass extinction at Meishan, South China. *Palaeogeography, Palaeoclimatology, Palaeoecology* **544**, 109626 (2020).

48. S. D. Burgess, S. Bowring, S.-z. Shen, High-precision timeline for Earth's most severe extinction. *Proceedings of the National Academy of Sciences* **111**, 3316-3321 (2014).
49. R. T. Barber, F. P. Chavez, Biological Consequences of El Niño. *Science* **222**, 1203-1210 (1983).
50. S. Xie *et al.*, Changes in the global carbon cycle occurred as two episodes during the Permian Triassic crisis. *Geology* **35**, 1083-1086 (2007).
51. S.-z. Shen *et al.*, High-resolution $\delta^{13}C_{carb}$ chemostratigraphy from latest Guadalupian through earliest Triassic in South China and Iran. *Earth and Planetary Science Letters* **375**, 156-165 (2013).
52. S. E. Grasby *et al.*, Isotopic signatures of mercury contamination in latest Permian oceans. *Geology* **45**, 55-58 (2017).
53. M. M. Joachimski *et al.*, Five million years of high atmospheric CO_2 in the aftermath of the Permian-Triassic mass extinction. *Geology* **50**, 650-654 (2022).
54. J. Wu *et al.*, Stepwise deforestation during the Permian-Triassic boundary crisis linked to rising temperatures. *Earth and Planetary Science Letters* **620**, 118350 (2023).
55. F. Yang *et al.*, Collapse of Late Permian chert factories in equatorial Tethys and the nature of the Early Triassic chert gap. *Earth and Planetary Science Letters* **600**, 117861 (2022).
56. M. M. Joachimski *et al.*, Devonian climate and reef evolution: Insights from oxygen isotopes in apatite. *Earth and Planetary Science Letters* **284**, 599-609 (2009).
57. E. Pucéat *et al.*, Revised phosphate-water fractionation equation reassessing paleotemperatures derived from biogenic apatite. *Earth and Planetary Science Letters* **298**, 135-142 (2010).
58. S.-z. Shen *et al.*, Calibrating the End-Permian Mass Extinction. *Science* **334**, 1367-1372 (2011).
59. J. Haslett, A. Parnell, A simple monotone process with application to radiocarbon-dated depth chronologies. *Journal of the Royal Statistical Society: Series C (Applied Statistics)* **57**, 399-418 (2008).
60. C.-q. Cao, Q.-f. Zheng, High-resolution lithostratigraphy of the Changhsingian Stage in Meishan section D, Zhejiang. *Journal of Stratigraphy* **31**, 14-22 (2007).
61. S. N. Wood, Fast stable restricted maximum likelihood and marginal likelihood estimation of semiparametric generalized linear models. *Journal of the Royal Statistical Society: Series B (Statistical Methodology)* **73**, 3-36 (2011).
62. P. J. Valdes *et al.*, The BRIDGE HadCM3 family of climate models: HadCM3@Bristol v1.0. *Geoscientific Model Development* **10**, 3715-3743 (2017).
63. P. J. Valdes, C. R. Scotese, D. J. Lunt, Deep ocean temperatures through time. *Climate of the Past* **17**, 1483-1506 (2021).
64. A. Farnsworth *et al.*, Past East Asian monsoon evolution controlled by paleogeography, not CO_2. *Science Advances* **5**, eaax1697 (2019).
65. L. A. Jones, P. D. Mannion, A. Farnsworth, F. Bragg, D. J. Lunt, Climatic and tectonic drivers shaped the tropical distribution of coral reefs. *Nature Communications* **13**, 3120 (2022).
66. P. M. Cox *et al.*, The impact of new land surface physics on the GCM simulation of climate and climate sensitivity. *Climate Dynamics* **15**, 183-203 (1999).
67. J. T. Kiehl, C. A. Shields, Sensitivity of the Palaeocene–Eocene Thermal Maximum climate to cloud properties. *Philosophical Transactions of the Royal Society A: Mathematical, Physical and Engineering Sciences* **371**, 20130093 (2013).
68. N. Sagoo, P. Valdes, R. Flecker, L. J. Gregoire, The Early Eocene equable climate problem: can perturbations of climate model parameters identify possible solutions? *Philosophical*

Transactions of the Royal Society A: Mathematical, Physical and Engineering Sciences **371**, 20130123 (2013).
69. M. D. Cox, A primitive equation, 3-dimensional model of the ocean. *GFDL ocean group technical report* **1**, (1984).
70. M. Collins, S. F. B. Tett, C. Cooper, The internal climate variability of HadCM3, a version of the Hadley Centre coupled model without flux adjustments. *Climate Dynamics* **17**, 61-81 (2001).
71. A. Farnsworth *et al.*, Climate sensitivity on geological timescales controlled by nonlinear feedbacks and ocean circulation. *Geophysical Research Letters* **46**, 9880-9889 (2019).
72. R. Joseph, S. Nigam, ENSO evolution and teleconnections in IPCC's twentieth-century climate simulations: Realistic representation? *Journal of Climate* **19**, 4360-4377 (2006).
73. G. L. Foster, D. L. Royer, D. J. Lunt, Future climate forcing potentially without precedent in the last 420 million years. *Nature Communications* **8**, 14845 (2017).
74. D. Gough, in *Physics of Solar Variations: Proceedings of the 14th ESLAB Symposium held in Scheveningen, The Netherlands, 16–19 September, 1980*. (Springer, 1981), pp. 21-34.
75. J. O. Kaplan *et al.*, Climate change and Arctic ecosystems: 2. Modeling, paleodata-model comparisons, and future projections. *Journal of Geophysical Research: Atmospheres* **108**, (2003).
76. C. J. R. Williams *et al.*, African Hydroclimate During the Early Eocene From the DeepMIP Simulations. *Paleoceanography and Paleoclimatology* **37**, e2022PA004419 (2022).
77. S.-F. Li *et al.*, Orographic evolution of northern Tibet shaped vegetation and plant diversity in eastern Asia. *Science Advances* **7**, eabc7741.
78. J. L. Brown, D. J. Hill, A. M. Dolan, A. C. Carnaval, A. M. Haywood, PaleoClim, high spatial resolution paleoclimate surfaces for global land areas. *Scientific Data* **5**, 180254 (2018).
79. A. Farnsworth *et al.*, Paleoclimate model-derived thermal lapse rates: Towards increasing precision in paleoaltimetry studies. *Earth and Planetary Science Letters* **564**, 116903 (2021).
80. J. N. Bahcall, M. H. Pinsonneault, S. Basu, Solar Models: Current Epoch and Time Dependences, Neutrinos, and Helioseismological Properties. *The Astrophysical Journal* **555**, 990 (2001).
81. N. Preto, E. Kustatscher, P. B. Wignall, Triassic climates—State of the art and perspectives. *Palaeogeography, Palaeoclimatology, Palaeoecology* **290**, 1-10 (2010).
82. E. Hawkins, R. Sutton, The potential to narrow uncertainty in regional climate predictions. *Bulletin of the American Meteorological Society* **90**, 1095-1108 (2009).
83. H. Zhang *et al.*, The terrestrial end-Permian mass extinction in South China. *Palaeogeography, Palaeoclimatology, Palaeoecology* **448**, 108-124 (2016).
84. K. Jewuła, W. Trela, A. Fijałkowska-Mader, Sedimentary and pedogenic record of seasonal humidity during the Permian-Triassic transition on the SE margin of Central European Basin (Holy Cross Mountains, Poland). *Palaeogeography, Palaeoclimatology, Palaeoecology* **564**, 110154 (2021).
85. D. C. G. Ravidà, L. Caracciolo, S. Henares, M. Janssen, H. Stollhofen, Drainage and environmental evolution across the Permo-Triassic boundary in the south-east Germanic Basin (north-east Bavaria). *Sedimentology* **69**, 501-536 (2022).
86. M. Hiete, H.-G. Röhling, C. Heunisch, U. Berner, Facies and climate changes across the Permian–Triassic boundary in the North German Basin: insights from a high-resolution organic carbon isotope record. *Geological Society, London, Special Publications* **376**, 549-574 (2013).

87. F. Käsbohrer, J. Kuss, Lower Triassic (Induan) stromatolites and oolites of the Bernburg Formation revisited–microfacies and palaeoenvironment of lacustrine carbonates in Central Germany. *Facies* **67**, 1-31 (2021).
88. A. J. Newell, V. P. Tverdokhlebov, M. J. Benton, Interplay of tectonics and climate on a transverse fluvial system, Upper Permian, Southern Uralian Foreland Basin, Russia. *Sedimentary Geology* **127**, 11-29 (1999).
89. A. J. Newell *et al.*, Disruption of playa–lacustrine depositional systems at the Permo-Triassic boundary: evidence from Vyazniki and Gorokhovets on the Russian Platform. *Journal of the Geological Society* **167**, 695-716 (2010).
90. A. J. Newell *et al.*, Calcretes, fluviolacustrine sediments and subsidence patterns in Permo-Triassic salt-walled minibasins of the south Urals, Russia. *Sedimentology* **59**, 1659-1676 (2012).
91. Z. Zhu *et al.*, Altered fluvial patterns in North China indicate rapid climate change linked to the Permian-Triassic mass extinction. *Scientific Reports* **9**, 16818 (2019).
92. Z. Zhu *et al.*, Intensifying aeolian activity following the end-Permian mass extinction: Evidence from the Late Permian–Early Triassic terrestrial sedimentary record of the Ordos Basin, North China. *Sedimentology* **67**, 2691-2720 (2020).
93. C. Davies, M. B. Allen, M. M. Buslov, I. Safonova, Deposition in the Kuznetsk Basin, Siberia: Insights into the Permian–Triassic transition and the Mesozoic evolution of Central Asia. *Palaeogeography, Palaeoclimatology, Palaeoecology* **295**, 307-322 (2010).
94. S. Mishra, N. Aggarwal, N. Jha, Palaeoenvironmental change across the Permian-Triassic boundary inferred from palynomorph assemblages (Godavari Graben, south India). *Palaeobiodiversity and Palaeoenvironments* **98**, 177-204 (2018).
95. R. M. H. Smith, Changing fluvial environments across the Permian-Triassic boundary in the Karoo Basin, South Africa and possible causes of tetrapod extinctions. *Palaeogeography, Palaeoclimatology, Palaeoecology* **117**, 81-104 (1995).
96. M. R. Gibling, R. Jia, R. A. Gastaldo, J. Neveling, H. Rochín-Bañaga, Braided-river architecture of the Triassic Swartberg member, Katberg formation, South Africa: Assessing age, fluvial style, and paleoclimate after the end-Permian extinction. *Journal of Sedimentary Research* **93**, 741-775 (2023).
97. J. Botha *et al.*, New geochemical and palaeontological data from the Permian-Triassic boundary in the South African Karoo Basin test the synchronicity of terrestrial and marine extinctions. *Palaeogeography, Palaeoclimatology, Palaeoecology* **540**, 109467 (2020).
98. M. F. Miller, J. W. Collinson, Trace fossils from Permian and Triassic sandy braided stream deposits, Central Transantarctic Mountains. *Palaios* **9**, 605-610 (1994).
99. C. R. Fielding *et al.*, Sedimentology of the continental end‐Permian extinction event in the Sydney Basin, eastern Australia. *Sedimentology* **68**, 30-62 (2021).
100. S. McLoughlin, S. Lindström, A. N. Drinnan, Gondwanan floristic and sedimentological trends during the Permian–Triassic transition: new evidence from the Amery Group, northern Prince Charles Mountains, East Antarctica. *Antarctic Science* **9**, 281-298 (1997).
101. D. C. G. Ravidà, L. Caracciolo, W. A. Heins, H. Stollhofen, Reconstructing environmental signals across the Permian-Triassic boundary in the SE Germanic basin: Paleodrainage modelling and quantification of sediment flux. *Global and Planetary Change* **206**, 103632 (2021).
102. L. Caracciolo *et al.*, Reconstructing environmental signals across the Permian-Triassic boundary in the SE Germanic Basin: A Quantitative Provenance Analysis (QPA) approach. *Global and Planetary Change*, 103631 (2021).

103. Q. Wu *et al.*, The terrestrial end-Permian mass extinction in the paleotropics postdates the marine extinction. *Science Advances* **10**, eadi7284 (2024).
104. P. Nutiprapun *et al.*, Effects of El Niño drought on seedling dynamics in a seasonally dry tropical forest in Northern Thailand. *Global Change Biology* **29**, 451-461 (2023).
105. W. Yang *et al.*, Paleoenvironmental and paleoclimatic evolution and cyclo- and chrono-stratigraphy of upper Permian–Lower Triassic fluvial-lacustrine deposits in Bogda Mountains, NW China — Implications for diachronous plant evolution across the Permian–Triassic boundary. *Earth-Science Reviews* **222**, 103741 (2021).
106. V. P. Tverdokhlebov, G. I. Tverdokhlebova, A. V. Minikh, M. V. Surkov, M. J. Benton, Upper Permian vertebrates and their sedimentological context in the South Urals, Russia. *Earth-Science Reviews* **69**, 27-77 (2005).
107. T. Kearsey, R. J. Twitchett, A. J. Newell, The origin and significance of pedogenic dolomite from the Upper Permian of the South Urals of Russia. *Geological Magazine* **149**, 291-307 (2012).
108. G. K. Taylor *et al.*, Magnetostratigraphy of Permian/Triassic boundary sequences in the Cis-Urals, Russia: No evidence for a major temporal hiatus. *Earth and Planetary Science Letters* **281**, 36-47 (2009).
109. F. Scholze *et al.*, A multistratigraphic approach to pinpoint the Permian-Triassic boundary in continental deposits: The Zechstein–Lower Buntsandstein transition in Germany. *Global and Planetary Change* **152**, 129-151 (2017).
110. J. W. Schneider, R. Rössler, R. Werneburg, F. Scholze, S. Voigt, paper presented at the CPC-2014 Field Meeting on Carboniferous and Permian Nonmarine–Marine Correlation, Freiberg, Germany, 2014.
111. M. J. Benton, A. J. Newell, Impacts of global warming on Permo-Triassic terrestrial ecosystems. *Gondwana Research* **25**, 1308-1337 (2014).
112. S. Bourquin *et al.*, The Permian–Triassic transition and the onset of Mesozoic sedimentation at the northwestern peri-Tethyan domain scale: Palaeogeographic maps and geodynamic implications. *Palaeogeography, Palaeoclimatology, Palaeoecology* **299**, 265-280 (2011).
113. J. Bodnar, E. P. Coturel, J. I. Falco, M. Beltrán, An updated scenario for the end-Permian crisis and the recovery of Triassic land flora in Argentina. *Historical Biology* **33**, 3654-3672 (2021).
114. G. Cornamusini *et al.*, A lithostratigraphic reappraisal of a Permian-Triassic fluvial succession at Allan Hills (Antarctica) and implications for the terrestrial end-Permian extinction event. *Palaeogeography, Palaeoclimatology, Palaeoecology* **627**, 111741 (2023).
115. S. G. Thomas *et al.*, Palaeosol stratigraphy across the Permian–Triassic boundary, Bogda Mountains, NW China: Implications for palaeoenvironmental transition through earth's largest mass extinction. *Palaeogeography, Palaeoclimatology, Palaeoecology* **308**, 41-64 (2011).
116. A. Bercovici, Y. Cui, M.-B. Forel, J. Yu, V. Vajda, Terrestrial paleoenvironment characterization across the Permian–Triassic boundary in South China. *Journal of Asian Earth Sciences* **98**, 225-246 (2015).
117. J. H. Powell *et al.*, The Permian -Triassic Boundary, Dead Sea, Jordan: Transitional alluvial to marine depositional sequences and biostratigraphy. *Rivista Italiana di Paleontologia e Stratigrafia* **122**, 23-40 (2016).
118. N. Benaouiss, A. Tourani, S. Bourquin, N.-E. Jalil, Late Permian to early Middle Triassic palaeoenvironmental reconstructions of the High Atlas, Morocco: Geodynamic and climate implications in the intertropical western Peri-Tethyan domain. *Palaeogeography, Palaeoclimatology, Palaeoecology* **630**, 111809 (2023).

119. A. Wilson, S. Flint, T. Payenberg, E. Tohver, L. Lanci, Architectural styles and sedimentology of the fluvial Lower Beaufort Group, Karoo Basin, South Africa. *Journal of Sedimentary Research* **84**, 326-348 (2014).
120. N. J. Tabor *et al.*, Evidence of a continuous continental Permian-Triassic boundary section in western equatorial Pangea, Palo Duro Basin, Northwest Texas, U.S.A. *Frontiers in Earth Science* **9**, 747777 (2022).
121. H. S. Jiang *et al.*, Restudy of conodont zonation and evolution across the P/T boundary at Meishan section, Changxing, Zhejiang, China. *Global and Planetary Change* **55**, 39-55 (2007).

Acknowledgements
Mike Orchard is thanked for providing conodont specimens from Idaho. Johann Müller and Nussaïbah Raja helped with the Bayesian age model and generalized additive models. Vladimir V. Silantiev, Fedor A. Mouraviev, Daoliang Chu and Wenchao Shu helped in the field.

Funding:

National Natural Science Foundation of China grants 41821001, 42272022 (YDS)

Deutsche Forschungsgemeinschaft Research Unit TERSANE FOR 2332: Temperature-related stressors as a unifying principle in ancient extinctions; Project Jo 219/15 (MMJ)

Natural Environment Research Council NE/J01799X/1, NE/V001639/1 (DPGB)

Author contributions:

Conceptualization: YDS, AF

Methodology: MMJ, PJV

Investigation: YDS, AF, MMJ, PBW, LK, DPGB, DCGR

Visualization: YDS, AF, DCGR

Funding acquisition: YDS, AF, MMJ, DPGB

Supervision: MMJ, PJV

Writing – original draft: YDS

Writing – review & editing: PBW, AF, MMJ, DPGB, LK

Competing interests: Authors declare that they have no competing interests.

Data and materials availability: All data are available in the main text or the supplementary materials.

Supplementary Materials

Materials and Methods

Supplementary text

Figs. S1 to S18

Tables S1 to S5

References (*56*–*121*)

Figure captions

Fig. 1 Evolution of the low latitude zonal SST gradient and summary of marine and terrestrial changes across the Permian-Triassic transition. (**A**) Modelled annual mean SSTs of the Changhsingian oceans with 857 ppm pCO_2 forcing. The black rectangle highlights the Niño 3.4 equivalent region for diagnosing ENSO signals. Study sites: Meishan and Laren (China), Vigil (Italy), Mućˊ (Croatia), Georgetown (USA), Kuh-e-Ali Bashi (Iran) and Chanakhchi (Armenia). (**B**) A sharp decrease in the zonal SST gradient across the Tethys from the late Permian to the Early Triassic. The solid black line represents the Locfit analysis of zonal SST gradient data (time window 0.2 Myr, alpha =0.4), with dashed lines bracketing the ±95% confidence interval. Due to uncertainties in paleogeographic reconstruction and sampling sites availability, the zonal SST gradient in equatorial Tethys was primarily calculated from sections between latitudes of 0.5° S and 10° N. (**C**) Carbon isotopes, Tethyan zonal SST gradient, and marine and terrestrial changes across the P-T transition. Siberian Traps eruptions, U-Pb radiometric ages, Hg peak and carbon isotopes (solid blue circles and open diamonds) from the Meishan stratotype section are from (*1, 48, 50-52*). Purple arrows indicate modelled SSTs reproduced in model simulations with 412, 857, 1712, 2568, and 4000 ppm pCO_2 (*53*). The high-resolution Tethyan zonal SST gradient was generated using a generalized additive model (*18*). Charcoal number, macroplant species in equatorial peatlands and correlations between marine and terrestrial P-T records are from (*11, 54*). The last occurrences of Permian reefs, radiolarian species and the chert gaps are from (*43, 44, 46, 55*). Our simulations suggest that MOC (meridional overturning circulation) collapsed as pCO_2 doubled from 412 to 857 ppm. Ocean anoxia developed both in the deep ocean and epicontinental seas.

Fig. 2 Walker circulation (m/s) from each simulation through the Permian-Triassic transition. Positive values indicate descending movements and negative values indicate ascending movements. The Walker circulation weakened during the P-T transition, whilst both ascending and descending limbs contracted towards central Panthalassa.

Fig. 3 Equatorial SST anomalies. Data were calculated from 120 °W to 170 °W longitude and 5 °S to 5 °N latitude (derived from EOF analysis, where EOF1 explains >50% of variance), showing that the intensity and longevity of El Niño-Southern Oscillation increase with atmospheric pCO_2. Red-shaded and blue-shaded areas represent positive and negative anomalies, respectively. Extremely high pCO_2 levels were not required to produce a >3 °C temperature anomaly (the red dashed line highlights the 4 °C anomaly).

Fig. 4 Composite analysis of five consecutive El Niños. Annual mean 1.5 m air temperature (**A-F**) and annual mean precipitation (**G-L**) anomalies during El Niño years, relative to the 100-year climate mean for each time period and pCO_2, in the pre-industrial world and the transition from the pre-crisis (412 ppm) to the peak (4000 ppm) of the P-T crisis world. Our simulations suggest a strong ocean-land teleconnection in low latitudes, with southern high latitudes also being vulnerable to El Niño impacts.

Fig. 5 The compound effect of elevated climate variability and mean state warming showing the rate of change in the Permian-Triassic transition. (**A**) Short-term sea surface temperature variability (dashed line) that is typically controlled by ENSO events. (**B**) A scenario of ~3.5 °C mean state warming over 5 kyr, occurring twice at 251.99 Ma and 251.93 Ma. (**C**) The

compounding effect. If the thermal tolerance of a hypothetical species is 31 °C (T_{max}), increased climate variability accelerates extinction compared to predictions based solely on mean state temperature increases.

Science
AAAS

Supplementary Materials for

Mega El Niño instigated the end-Permian mass extinction

Y.D. Sun, A. Farnsworth, M.M. Joachimski, P.B. Wignall, L. Krystyn, D.P.G. Bond, D.C.G. Ravidà, P.J. Valdes

Corresponding author: yadong.sun@cug.edu.cn

The PDF file includes:

Materials and Methods

Materials

Conodonts were used to reconstruct seawater temperatures since their nektonic nature means that paleotemperatures derived from their hard parts reflect the seawater, rather than seafloor or in-sediment temperatures. The measured specimens were sourced from the collections of Mike J. Orchard and Leopold Krystyn, with additional samples collected specifically for this study. These samples were extracted from the host rocks using various methods detailed below. Information about sampling sites is provided in Table S1.

Methods

Conodont extraction

Conodonts were extracted using one of two disintegrating methods depending on types of host rocks. For carbonates, rock chips were dissolved in a diluted acetic acid solution (<10%) buffered by calcium phosphate. Conodonts were washed out along with coarse residuals. L.K.'s conodonts were processed with formic acid. All measured conodonts were screened under a binocular microscope, and most of them were also imaged by SEM to confirm good preservation. Control tests revealed that the extraction methods have no observable effect on oxygen isotope measurements.

Oxygen isotopes on conodont biogenic apatite ($\delta^{18}O_{PO4}$)

The PO_4^{3-} group in biogenic apatite was isolated and precipitated as Ag_3PO_4 following the procedure described in (*56*). Mono-generic conodont samples and laboratory standards (0.5-1.0 mg) were dissolved in 2 M HNO_3, neutralized with 2 M KOH and subjected to Ca^{2+} removal as CaF_2 using 2 M HF and centrifugation. Ag_3PO_4 was obtained by adding a silver amine solution to the clear supernatant solutions, followed by washing and drying. The resulting Ag_3PO_4 was homogenized and packed into silver foils. $\delta^{18}O_{PO4}$ analyses were performed using a TC-EA coupled online to a ThermoFisher Delta Plus V isotope ratio mass spectrometer (IRMS). Both samples and standards were typically measured in triplicate. All values are calibrated to the standard NBS 120c (21.7 ‰ VSMOW). External reproducibility, monitored by replicate analyses of the NBS 120c standard, was ±0.14 ‰ (1 σ, n=20). Internal reproducibility, monitored by replicate analyses of the samples, was ±0.03–0.20 ‰ (1 σ).

Calculation of paleotemperature from $\delta^{18}O_{PO4}$

The paleotemperature was calculated using the equation from ref (*57*) and assuming the Early Triassic oceans were ice-free with $\delta^{18}O_{seawater}$ = -1 ‰ VSMOW.

Establishment of a temporal framework for the Permian-Triassic (P-T) transition

The precise timing of the latest Permian environmental changes is built upon high-resolution U-Pb dating of the Meishan GSSP section (*48, 58*). We employed Bayesian statistics to estimate depositional durations of P-T beds at Meishan, including uncertainties. A time and depth model was built using the method and R-coding described in ref (*59*), with age input from (*48*) and bed thicknesses of the Meishan D section from (*60*). The 0 m level is assigned to the top of Bed 34 (Tables S2, S3).

Calculation of P-T zonal SST gradient along the paleoequator from proxy data

The zonal sea surface temperature (SST) gradient along the paleoequator was determined by calculating the maximum SST difference between western Tethyan sites [e.g., Alps, Armenia (*20*), and Iran (*19*)], eastern Tethyan sites [basins in South China (*4, 39*)], and a western Laurentian site (Idaho). Only data acquired using high-precision gas source IRMS were included in zonal SST calculations to avoid introducing analytical offset. Most of the Upper Permian sites used for the zonal SST reconstruction fell within a narrow band between approximately 0.5°S to 5°N. As most Tethyan microblocks drifted northward during the Early Triassic, sampling sites were between 0° and 10°N latitude.

For high-resolution zonal SST gradient records during the P-T transitional interval (shown in Fig. 1C), an algorithm was employed to interpolate values between eastern and western Tethys SST records. Generalized additive models, using the mgcv package (*61*), were applied to the SST data over time. The generated models were then used to predict temperature values at 10 kyr increments between ages 251.84 and 252.07 Ma and 5 kyr between ages 252.02 and 251.91 Ma. The resulting data are presented in Table S4.

Uncertainties of deep-time fossil and proxy data

The fossil record of deep time is incomplete, which is obvious in marine settings and prominent in terrestrial basins. Ancient sea floors (> ~150 Ma) were largely subducted into the mantle, limiting sampling sites of deep-time studies to epicontinental seas. Only a handful of P-T basins have good marine sedimentary records, robust age controls and credible proxy records. Most of these basins were situated in the low latitudes.

Conodonts used for oxygen isotope analysis are rare and challenging to extract, rendering SST reconstruction for the P-T time a labor endeavor. Only a handful of SST records for the studied interval exist.

These factors limit our understanding of past faunal and floral changes and our ability to compare modelling outputs with fossil and proxy records more effectively.

Earth System modelling

To explore whether both paleoclimatic and paleoweather conditions influenced global extinction events across the P-T boundary, we utilized a newly updated version of a state-of-the-art paleo-General Circulation Model (GCM).

i) Paleoclimate model

Paleoclimate model simulations were carried out using a recent version of the UK MetOffice coupled Atmosphere-Ocean General Circulation Model (AOGCM), HadCM3L-M2.1D (*62*) with a model resolution of 3.75° longitude × 2.5° latitude in the atmosphere and ocean (~250 km grid squares in the tropics). The HadCM3 family of models has extensively contributed to the Coupled Model Intercomparison Project (CMIP 1-5) experiments, as well as the Paleoclimate Modelling Intercomparison Project (PMIP 1-4), showcasing proficiency in reproducing both modern (*62*) and paleoclimate (*63-65*) conditions. Standard in climate models, sub-grid processes like cloud, convection, and oceanic eddies are parameterized due to resolution limitations.

Due to a lack of geological spatiotemporal data recording land surface vegetation and soil characteristics, in particular for deep time climates such as the P-T, we use a predictive interactive vegetation scheme using modern expressions for broadleaf trees, deciduous trees, shrubs, and grasses and a globally uniform distribution of a medium loam soil characteristics in the model land surface scheme (MOSES 2.1)(*66*). The land surface scheme also includes evaporation from sub-grid scale lakes (which are prescribed as a lake fraction in each grid box at the start of the simulation). Critically, we use a version of the model that includes the dynamical vegetation model TRIFFID (Top-Down Representation of Interactive Foliage and Flora Including Dynamics). TRIFFID predicts the distribution and properties of global vegetation by employing plant functional types (PFTs) represented as fractional coverage within a grid-cell. These predictions are informed by competition equations grounded in the climate tolerance of the five PFTs. This is crucial because, unlike most other paleoclimate models that prescribe vegetation, vegetation patterns in our model emerge from the model physics. This results in more realistic land-surface atmosphere feedback for each scenario during the P-T, which is critical for understanding the pacing and timing of the extinction event.

A decades-old problem that persists today in most paleoclimate models is their inability to simulate higher latitude warmth during past warm periods as proxy evidence suggests (the so-called 'Cold Pole Paradox'). The HadCM3L-M2.1D model has a further update that includes modification to cloud condensation nuclei density and cloud droplet effective radius following recent work (*67, 68*). This raises higher latitude temperatures without significantly changing tropical temperatures, reducing the pole-to-equator temperature gradient in line with proxy observations. This update is also found to work under hot (Cretaceous), cool (Miocene) and icehouse (Last Glacial Maximum) conditions, as well as under pre-industrial boundary conditions, making it appropriate for use across all periods of the Phanerozoic.

The ocean model is based on the model of Cox et al. (*69*) and is a full primitive equation, 3D model of the ocean. A second-order numerical scheme is used along with centered advection to remove nonlinear instabilities. Flux adjustments (such as artificial heat and salinity adjustments in the ocean component model (*70*) to prevent it from drifting to unrealistic values) are not required in this model, which is crucial for long paleoclimate simulations (*71*). Models requiring flux adjustments were found to produce too little El Niño variability and a peak in variability in the central rather than eastern equatorial Pacific in the Modern (*72*), which is not desirable. Sea ice is calculated on a zero-layer model with partial coverage, and a consistent salinity is assumed for ice. Each simulation was initialized from an equilibrated pre-industrial state in the atmosphere and ocean.

To understand the impact of El Niño during the P-T boundary interval, it is essential that the model accurately reproduces El Niño Southern Oscillation (ENSO) characteristics. HadCM3 has one of the most realistic representations of El Niño amongst state-of-the-art paleoclimate prediction models in terms of strength, frequency, and phase locking of El Niño events (*72*).

ii) Snapshot simulations of specific boundary conditions and spin-up.

Eight 'snapshot' simulations with time-specific boundary conditions were conducted over the P-T boundary and pre-industrial period, using Getech Plc. paleogeographic reconstructions for the Changhsingian and the Induan. Each stage and time-specific DEM was interpolated from a 0.5° × 0.5° grid onto the HadCM3L 3.75° × 2.5° grid. 'Realistic' pCO_2 concentrations for each simulation are based on (*73*) and values estimated from a paleosol barometer (*53*) with the proxy uncertainty taken into consideration. Specifically, pCO_2 of 412 ppm, 857 ppm, 1,712 ppm and 2,568 ppm were chosen for the Changhsingian and 879 ppm and 4,000 ppm for the Induan.

Time-specific solar luminosity for each simulation was based on ref (*74*), while other boundary conditions (e.g., orbital parameters, volcanic aerosol concentrations, etc.) are held constant at pre-industrial values. To ensure each simulation has fully adjusted to the boundary conditions, we follow a 3-stage spin-up protocol so that each simulation is fully equilibrated: i) the globally and volume-integrated annual mean ocean temperature trend is less than 1°C per 1000 years, ii) trends in surface air temperature are less than 0.3°C per 1,000 years, and iii) net energy balance at the top of the atmosphere, averaged over a 100-year period at the end of the simulation, is less than 0.25/W m^2. These simulations have generally been run for over 10000 model years to ensure complete Earth system equilibrium.

Climate means [i.e., mean annual temperature (MAT), mean annual precipitation (MAP), sea surface temperature (SST), etc.] were produced from the last 100 years of the simulation.

Biome4 is an offline equilibrium coupled carbon and water flux vegetation model (*75*), which predicts the geographic distribution and quantitative properties of vegetation using the paleoclimate model simulations from this study. Biome4 requires knowledge of the climate (monthly mean temperature and precipitation), sunshine, and physical characteristics of the soil (soil texture and depth) to determine water holding capacity and percolation rates, as well as CO_2 concentrations in the atmosphere.

Biome4 has 12 plant functional types (PFTs) representing the physiology of modern vegetation classes from forests, shrubs to grasses. Each PFT is determined through a set of competition equations (e.g., bioclimatic limits) to determine occupancy. For further information, see Kaplan et al. (*75*). Although these modern PFTs were dissimilar to past vegetation types during the P-T, they likely represent the broad vegetation strategies that existed in the past, except for C4 vegetation, which, due to the warmer climate, has low occupancy in these simulations. Biome4 has been heavily utilized by various paleoclimate studies (*76*-*78*).

Uncertainties in Earth system modelling

Global proxy databases cover past time periods but become less constrained with diminishing spatiotemporal data into the geological past. This necessitates using paleoclimate models in conjunction with proxies to provide these global datasets. Paleoclimate simulations of deep-time climates are challenging. In part, this is because there are many uncertainties that need to be considered when undertaking a model simulation, which, depending on the time period, can be relatively unconstrained by proxy data. Uncertainties can be generally partitioned into two main sources: i) boundary condition uncertainty; and ii) model uncertainty.

i) Boundary conditions are spatiotemporally varying parameters that are required by climate models but cannot be calculated internally by the model and instead need to be provided by the user. The most important boundary conditions for the model used here are (a) paleogeographic reconstructions, (b) solar luminosity, (c) orbital configuration, and (d) greenhouse gas concentrations.

(a) **Paleogeographic reconstruction** is a significant source of uncertainty. DEMs, constrained by paleo-databases, provide topography, bathymetry, and land-sea concentration. These are crucial for determining local, regional, and global atmospheric and ocean circulation and, as a result, the underlying climate in the model. The further back in the geological record, the greater the reduction in the constraint of proxies, creating larger uncertainties in these reconstructions. However, our understanding of plate tectonics, spreading ridges, weathering rates, and basinal deposition allows, in general, an accurate first-order approximation of deep-time paleogeography. The largest uncertainties usually result from the height and depth of topographic and bathymetric surfaces and their spatial coverage because of proxy uncertainty (*79*). Multi-stage paleogeographic reconstruction is currently available from only two datasets, the PALEOMAP project and Getech Plc. Getech Plc is used in this study.

(b) **Solar luminosity**, essentially the amount of energy received by a planetary body from its parent star, is fairly well known. Gough (*74*) approximated the amount of energy based on a simple model based on the age of the parent star. Apart from the first 0.2 Gyr, this approximation is shown to agree well with observations (*80*).

(c) **Orbital configuration** - the eccentricity, obliquity, and precession of the planet's orbit around its parent star and rotation on its own axis can have a substantial impact on the seasonal and latitudinal climate signal, which, in turn, can lead to significant changes in

climate state (glacial to interglacial). This is due to ice sheet formation and associated changes in global atmospheric and oceanic response. For deep-time simulations, a modern orbital configuration is often imposed for several reasons. Firstly, chronological uncertainty in proxies, which the model aims to compare, often spans many orbital cycles. This may result in the proxy being more representative of a mean orbital state (akin to the modern day). Secondly, it makes it easier to understand how different a deep-time climate is compared to our modern climate. Thirdly, orbital variations have the greatest climatic impact where ice sheets can form, which partly reflects atmospheric pCO_2 levels and global temperatures.

At the P-T boundary, there were no known land ice sheets (*81*), resulting in negligible glacio-eustatic changes. While orbital forcing is unlikely to be the primary driver of the P-T extinction event, it may have amplified the effects. However, this aspect falls outside the scope of this study.

(d) **Greenhouse gas concentrations**, particularly pCO_2 concentrations, are highly variable throughout the geological past. Constraining deep-time pCO_2 concentrations is challenging due to factors such as proxy type, age, techniques, calibration uncertainty, and the limited number of records (*73*). While combining multiple proxy sources can improve the robustness of pCO_2 estimates, it may also introduce errors that produce a mean pCO_2 estimate. Time averaging is another issue; While, for the most part, paleogeography changes on geological timescales, pCO_2 concentrations can vary on hundreds to million-year timescales. We aim to test the predicted pCO_2 range using a paleosol pCO_2 bathometer across the P-T boundary (*53*) to understand the impact of increasing pCO_2 on extinction intensity. By running a range of pCO_2 experiments, we cover the total range of potential pCO_2 to lessen this uncertainty.

(e) **Vegetation**. The HadCM3 family of models uses modern PFTs as part of the interactive vegetation scheme and is used in this study to predict vegetation cover. However, vegetation during the P-T boundary will have been different from today. This could have an unquantifiable impact. The PFTs chosen here are, in many senses, generalists covering a broad range of characteristics of vegetation adapted for cool, warm, wet, and dry regions. This is preferable to other solutions, such as prescribing vegetation cover everywhere, such as 'shrubs', as has often been the case.

ii) Although all globally available paleoclimate models use the same well-known sets of equations to simulate the large-scale behavior of the atmosphere and ocean, results from different models can vary, particularly at the local and regional scales. This is due to the complexity of each model, resolution dependencies, spin-up and the applied initial state, and parameterizations used to approximate processes such as cloud formation that cannot be explicitly resolved at the grid-scale of all current paleoclimate models. In an ideal world, such paleoclimate simulations would be run by multiple paleoclimate modelling groups, as is done in the CMIP for near-future climate change studies.

Regrettably, addressing this fully is beyond the scope of this paper (our simulations took over a year on a supercomputer), and few paleoclimate models can perform such deep-time simulations. However, confidence in the robustness of our results can be obtained by the fact that

(a) the HadCM3 family of models, although 20 years older than many of its contemporaries, still compares well with models from the previous IPCC Coupled CMIP fifth assessment models (*62*);

(b) HadCM3L-M2.1D has seen continued development (*62*). The updated version of the model we used solves the 'Cold Pole Paradox' problem;

(c) our simulations, lasting over 6,000 model years, stand out as most paleoclimate simulations are limited to one or two thousand years due to high computational costs. However, it can take upward of 5,000 model years to truly allow a simulation to equilibrate to all the applied model forcings, in particular for the deep ocean (*63*), and as such, the global ocean circulation to be fully representative of the deep-time period;

(d) although model uncertainty is important to constrain, it has been shown that scenario uncertainty (i.e., the applied boundary conditions) is a larger source of error, at least for future climate simulations (*82*). Therefore, running as many pCO_2 sensitivity tests as possible is essential to constrain its impact on paleo-ENSO at the P-T boundary.

Supplementary Text

Impact of paleogeographic settings on proxy and modelling results

Owing to uncertainties in paleogeographic reconstruction, paleo-coordinate estimation, and the limited availability of sampling sites recording deep-time conditions, our proxy data do not strictly fall within the 5°N-5°S band in Tethys in the Early Triassic. Consequently, the calculated zonal SST gradients can only overestimate the actual zonal SST gradients along the palaeoequator. As equatorial warm pools expanded in the hothouse climate, SSTs likely became more uniform in tropical zones, as also shown in our modelling results (Fig. S1). Therefore, including studied sites up to ~10°N latitude has minimal impact on our proxy data interpretation. Proxy SST records from the Panthalassa are absent because all P-T seafloors have been completely subducted to the mantle.

On the other hand, paleogeographic reconstruction may profoundly impact the output of Earth system modelling. However, Pangaea's configuration remained stable throughout the study period, with no evidence of major orogeny across the P-T boundary. Thus, paleogeographic changes probably had minimal impact on our modelling output. This is corroborated by ocean potential temperatures at 5 m and 301 m in the Changhsingian (857 ppm) and Induan (879 ppm), which show no notable paleogeographic impacts. Instead, pCO_2 drives the climate (Figs. S1, S3).

ENSO signatures in Tethys and Panthalassa

The Pangea world consisted of two major oceans—Tethys and Panthalassa. ENSO signatures, measured by equatorial SST anomalies, were registered in both oceans, evidenced by proxy data in the Tethys and model simulations in the Panthalassa.

For Tethys, SST proxy data are well established (Fig. 1). However, a Nino 3.4 equivalent index has yet to be defined, hindering direct comparisons of ancient ENSO signatures with today's. Although the paleotemperature proxy data show consistently low equatorial zonal SST gradients for an extended period of time, the data do not have enough temporal resolution to access ENSO variations at decadal or finer scales.

For Panthalassa, the marine Nino 3.4 index shows no permanent El Niños even with 4,000 ppm pCO_2 forcing. Proxy data is lacking because of an absence of sedimentary records due to the subduction of ancient seafloors.

Whether the Tethyan and Panthalassan ENSO(s) were one integrated event or coupled/decoupled separate events requires future, in-depth investigation, with paleogeography being the largest uncertainty. Here, we tentatively treat it as a single, integrated global event. Nevertheless, the Panthalassan record is comparable to our current understanding of the ENSO concept because i) Panthalassa was the Proto-Pacific and shows great similarity to the modern Pacific, and ii) The Nino 3.4 index is defined the same as today.

Sedimentary changes on land across the P–T boundary

Changes in terrestrial sedimentation patterns were widespread and relatively uniform at the low and mid-latitudes of Pangea across the P-T boundary, while only minor or no variations in facies associations were observed at high latitudes. In most basins, the P-T transition is marked by the onset of fluvial sedimentation or a shift to higher-energy fluvial morphologies (e.g., braided rivers), driven by increasing climate instability.

In equatorial SW China, on the eastern margin of the Kandian High, upper Permian muddy coastal swamp and sandy, meandering fluvial facies gradually change to sandy-dominated, braided systems in the Lower Triassic (*83*). Further west, but at the same latitude, on the southeast margin of the Central European Basin Systems, Upper Permian meandering and sabkha depositional systems were replaced by Lower Triassic gravel-dominated braided drainages (*84, 85*). Such changes did not occur in northern Germany, where mudstone-dominated playa lake deposits persisted into the Lower Triassic (*86, 87*).

In the northern mid-latitude settings of the southern Urals (Russia), Upper Permian sandy distal fan and mudflat deposits are overlain by thick, Lower Triassic conglomeratic braided river facies (*88*). A similar evolution took place ~800 km away in the Russian Platform, where upper Permian playa-lacustrine beds are overlain by sandstone-dominated fluvial facies with interbedded aeolian deposits (*89, 90*). Similarly, in the Ordos Basin (North China), cross-bedded sandstones and mudstones that record meandering rivers in Upper Permian alluvial plains are abruptly succeeded by Lower Triassic sandy braided and interbedded aeolian depositional systems (*91, 92*).

The shift from meandering to gravel-dominated braided fluvial sequences is also seen further north in the Kuznetsk Basin of Siberia (*93*).

In Gondwana, the Upper Permian fluvio-lacustrine environments and peat-forming swamps in the Pranhita-Godavari Basin (southeast India) were replaced by Triassic high-energy river systems (*94*). Southern high latitudes witnessed the early demise of Upper Permian peatlands and the development of diverse facies in the Lower Triassic, but changes in fluvial style are less evident and somewhat controversial. In the Karoo Basin (South Africa), Late Permian floodplain-dominated meandering systems were replaced by braided river systems in the Lower Triassic (*31, 95*), although recent studies challenge this trend (*96*). Such change was gradual at least in some sites (e.g., *97*). In the Sydney Basin (southeast Australia), little change in fluvial style is observed in all locations where a conformable boundary contact is archived (*29*). Sheet-like sandstone bodies occur at several stratigraphic levels within the Permian, prior to the supposed abrupt boundary change. In the Central Transantarctic Mountains of Antarctica, braided fluvial systems were established in the Late Permian and persisted into the Early Triassic, with little or no change in the sedimentary architecture (*98, 99*). The typical red bed style sedimentation started high above the P-T boundary in both Sydney Basin and the Prince Charles Mountains of East Antarctica, (*29, 100*).

The cause(s) of sedimentary environmental changes on land across the P-T transition are debated. Previous studies invoke the global die-off of the riparian vegetation that led to riverbank destabilization and consequent increased sediment erosion (*31, 88*). Recent studies highlight establishing a positive water balance and increasing seasonal precipitation in the upland catchment areas (*29, 84-86, 101, 102*).

<u>El Niños, the compounding effect and the P-T deforestation</u>

The P-T deforestation was apparently diachronous, with southern deforestation occurring earlier than the demise of tropical rainforests and peatland (*8, 11, 54, 103*), and preceding the increase in SST. Our modeling of the deforestation process aligns well with the fossil record, highlighting the compounding effect of short-term climate anomalies and mean-state climate changes played a vital role in the early collapse of terrestrial ecosystems. As the BIOME4 vegetation model considers monthly mean temperature and precipitation, earlier deforestation in southern latitudes requires a combined compounding effect of warmth and altered precipitation. This is consistent with the observation that El Niño droughts significantly increase forest seeding mortality, even in forests well adapted to seasonally dry conditions (*104*).

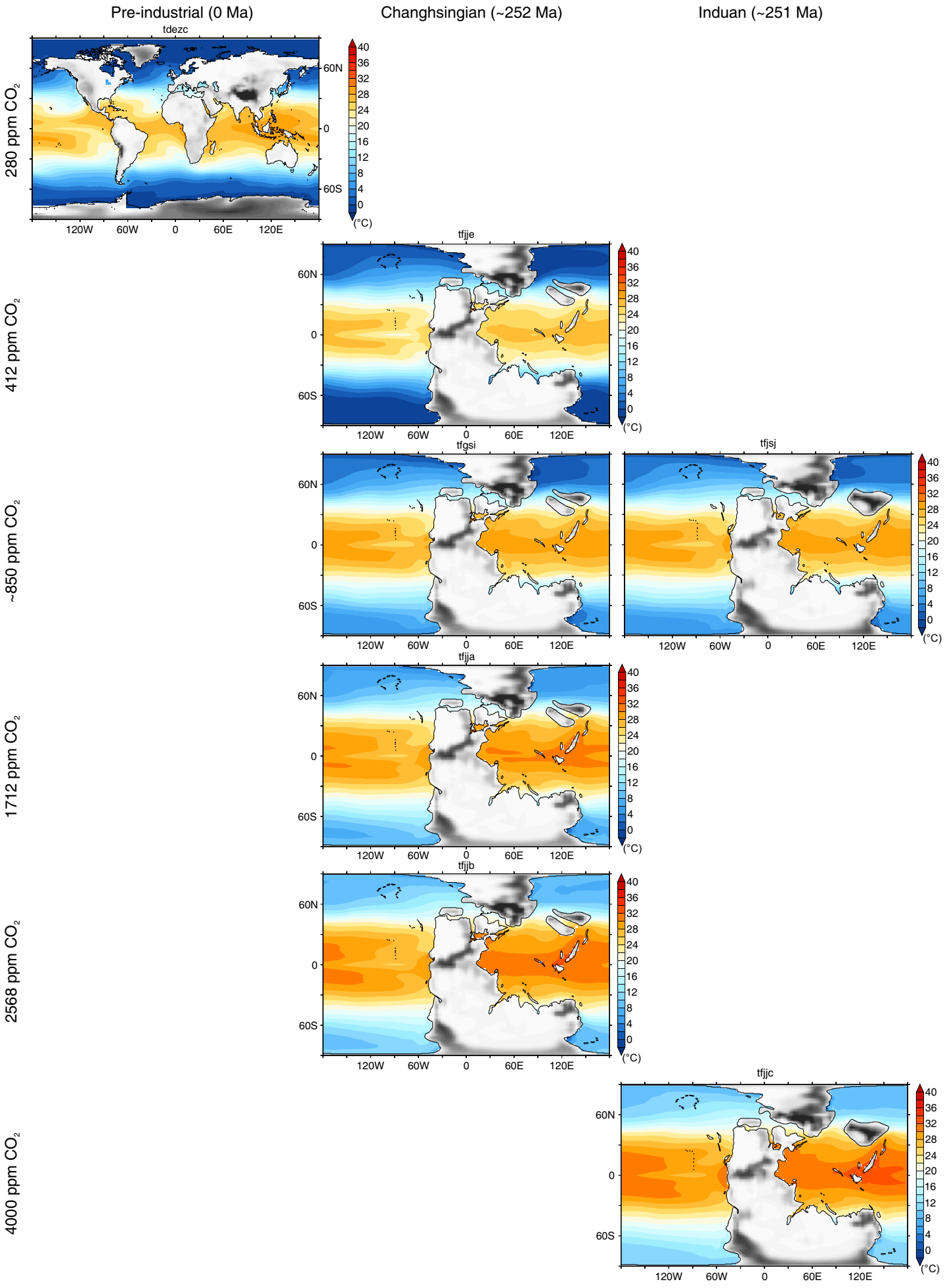
Pre-industrial (0 Ma)
Changhsingian (~252 Ma)
Induan (~251 Ma)
280 ppm CO2
412 ppm CO2
~850 ppm CO2
1712 ppm CO2
2568 ppm CO2
4000 ppm CO2
tdezc
tfjje
tfgsi
tfjsj
tfjja
tfjjb
tfjjc
60N
0
60S
120W
60W
0
60E
120E
40
36
32
28
24
20
16
12
8
4
0
(°C)

Fig. S1. Global mean annual sea surface temperature (°C) for each simulation for the pre-industrial period at 280 ppm (left column), Changhsingian ~252 Ma at 412 ppm, 857 ppm, 1712 ppm, and 2568 ppm (middle column), and Induan ~251 Ma at 879 ppm and 4000 ppm (right column) pCO_2, showing potent warming and the expansion of the equatorial warm pool across the P-T transition. Also note the potent warming of the cold tongue area in the western Pangea margin (approximately 5°N-5°S, 35°W).

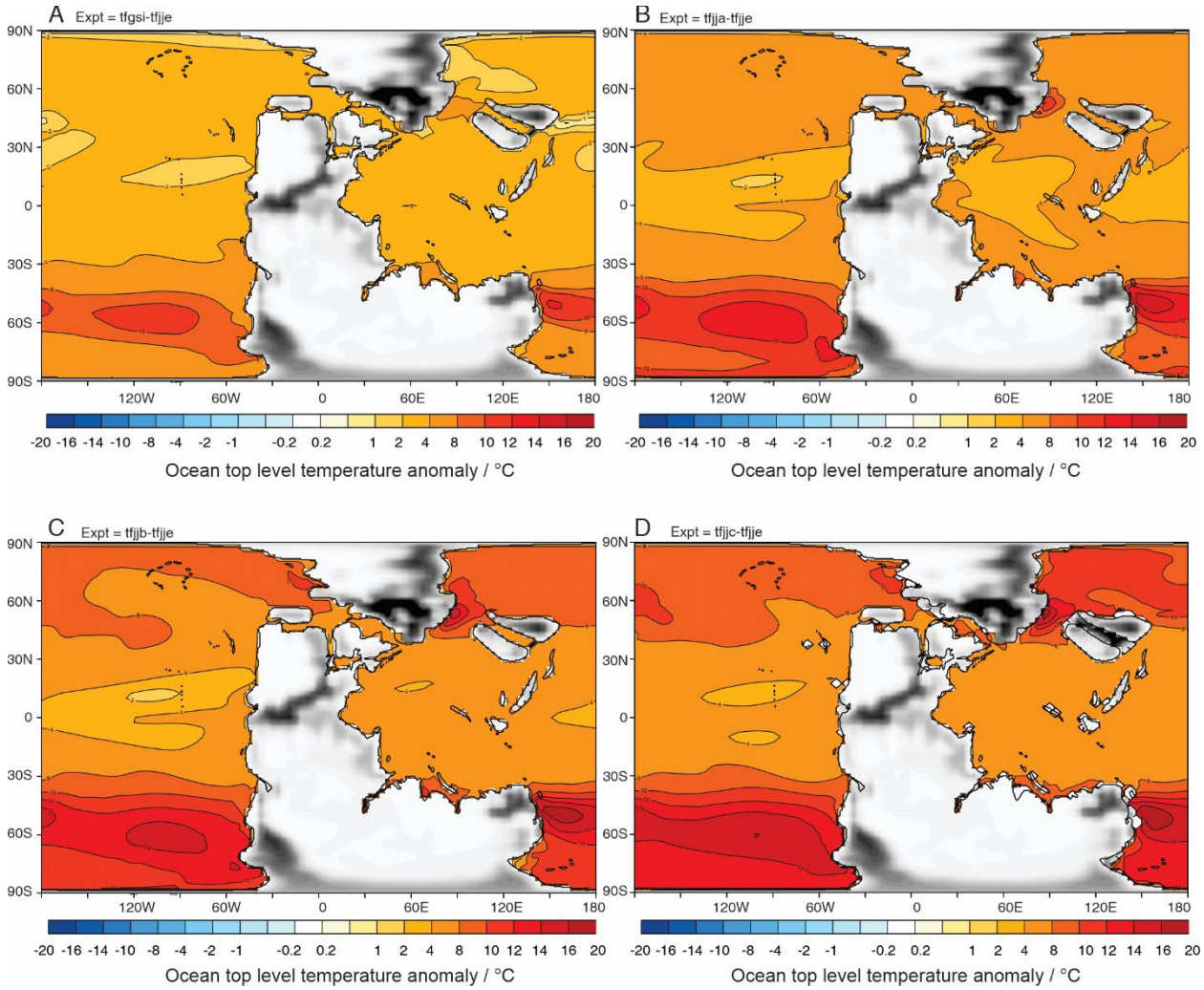

Fig. S2. Global mean annual sea surface temperature anomalies (°C) against the Changhsingian background state (412 ppm simulation). (A) SST anomalies between 857 ppm and 412 ppm simulations; (B) SST anomalies between 1712 ppm and 412 ppm simulations; (C) SST anomalies between 2568 ppm and 412 ppm simulations; (D) SST anomalies between 4000 ppm and 412 ppm simulations.

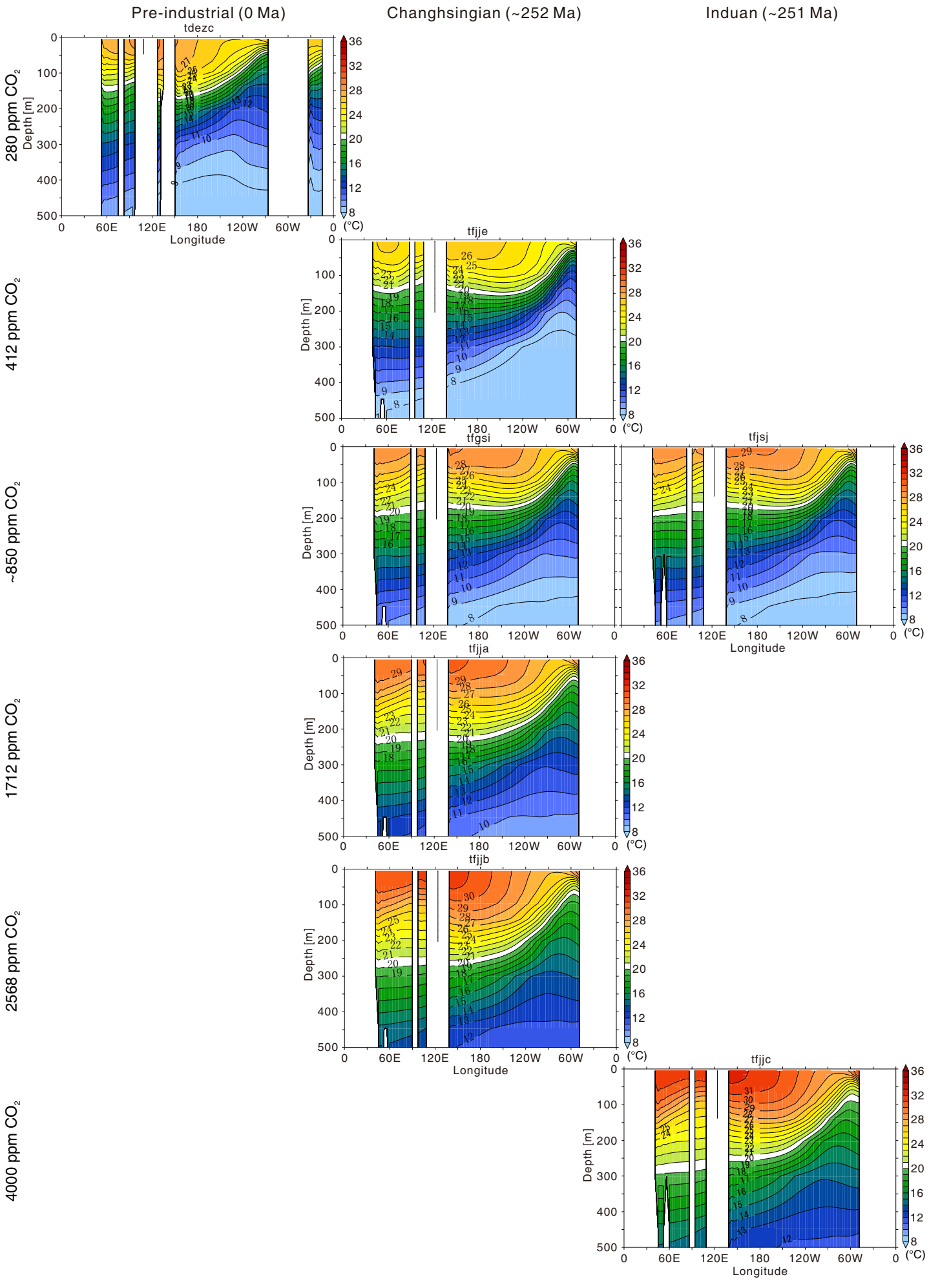
Pre-industrial (0 Ma)
Changhsingian (~252 Ma)
Induan (~251 Ma)
280 ppm CO2
412 ppm CO2
~850 ppm CO2
1712 ppm CO2
2568 ppm CO2
4000 ppm CO2
tdezc
tfjje
tfgsi
tfjsj
tfjja
tfjjb
tfjjc
Depth [m]
Longitude
(°C)

Fig. S3. Equatorial (10°N-10°S) mean annual ocean depth temperature profiles; 0-100 m (°C) for each simulation for the pre-industrial period at 280 ppm (left column), Changhsingian ~252 Ma at 412 ppm, 857 ppm, 1712 ppm, and 2568 ppm (middle column), and Induan ~251 Ma at 879 ppm and 4000 ppm (right column) pCO_2, showing a significant deepening of the thermocline across the P-T transition.

Pre-industrial (0 Ma)

Changhsingian (~252 Ma)

Induan (~251 Ma)

280 ppm CO_2

412 ppm CO_2

~850 ppm CO_2

1712 ppm CO_2

2568 ppm CO_2

4000 ppm CO_2

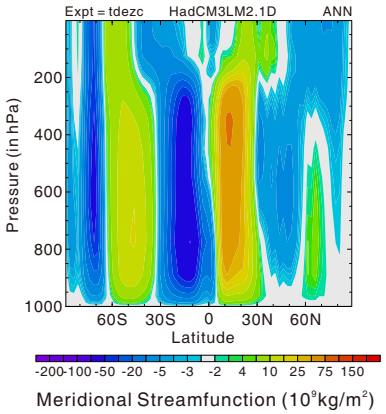

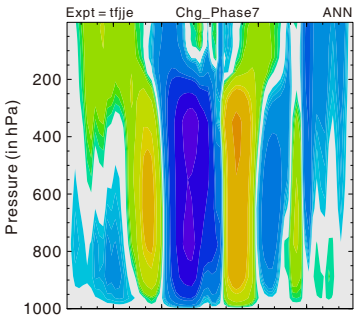

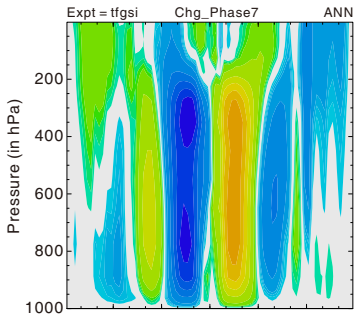

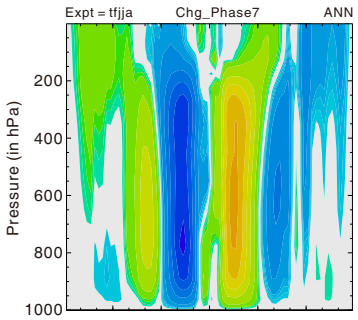

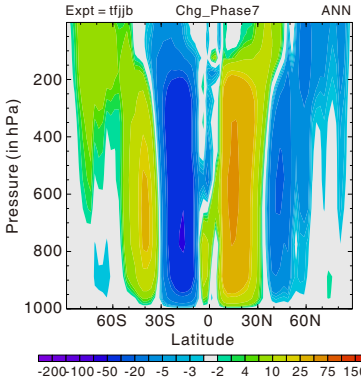

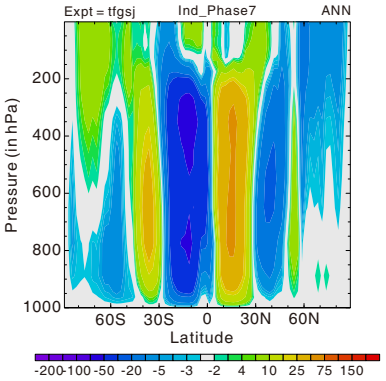

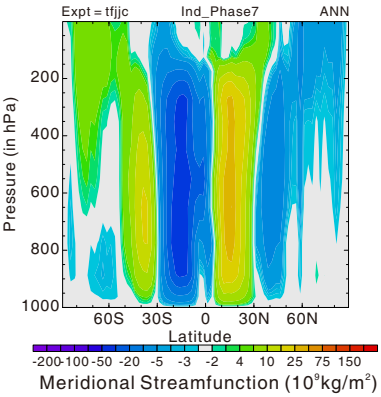

Fig. S4. Global zonally integrated mean annual atmospheric meridional stream function (kg/m2) for each simulation for the pre-industrial 280 ppm (left column), Changhsingian ~252 Ma at 412 ppm, 857 ppm, 1712 ppm, and 2568 ppm (middle column), and Induan ~251 Ma at 879 ppm and 4000 ppm (right column) pCO_2. Positive contour values indicate clockwise rotation whilst negative contour values indicate anti-clockwise rotation.

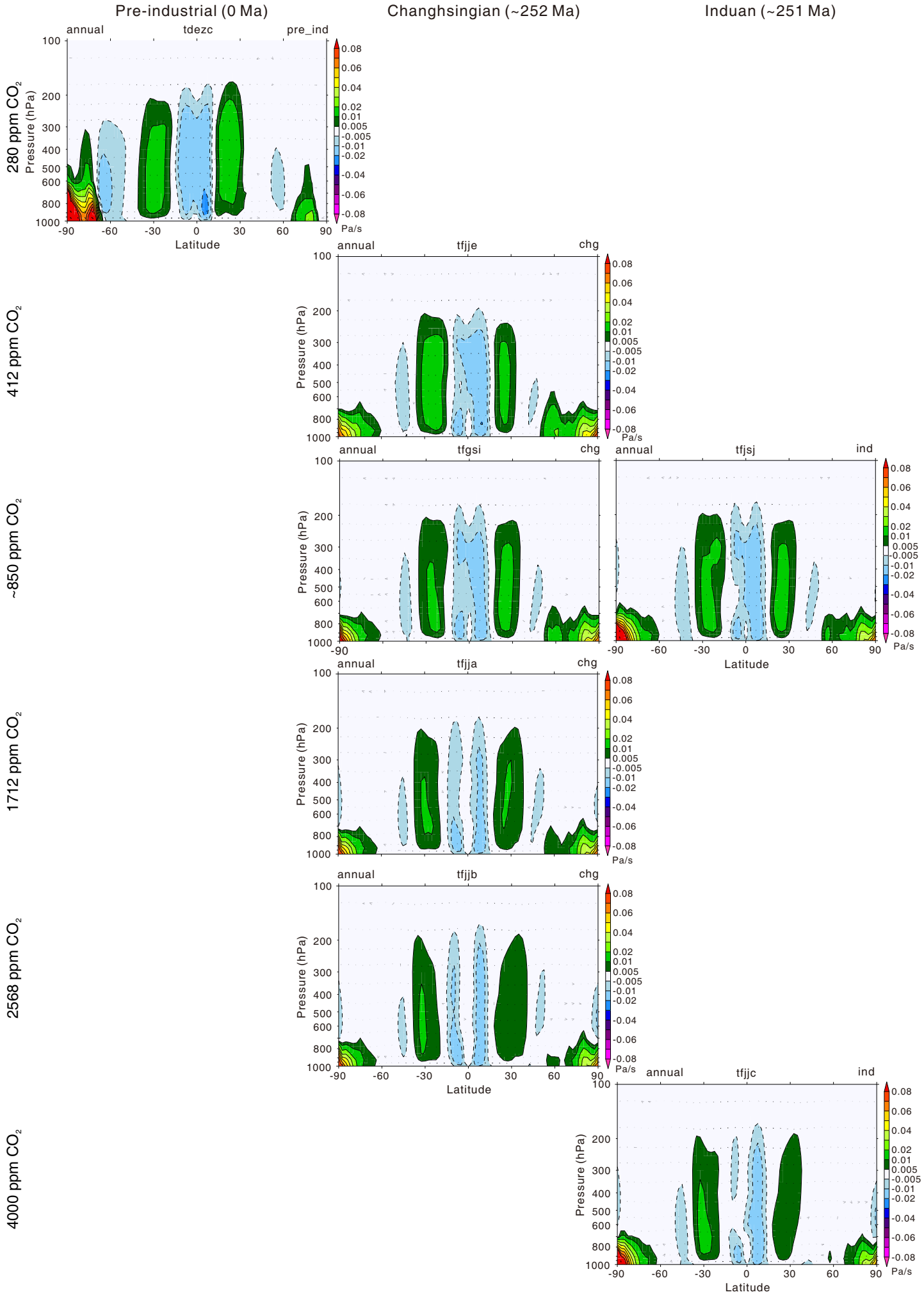
Pre-industrial (0 Ma)
Changhsingian (~252 Ma)
Induan (~251 Ma)
280 ppm CO2
412 ppm CO2
~850 ppm CO2
1712 ppm CO2
2568 ppm CO2
4000 ppm CO2
annual
tdezc
pre_ind
tfjje
chg
tfgsi
tfjsj
ind
tfjja
tfjjb
tfjjc
Pressure (hPa)
Latitude
Pa/s
100
200
300
400
500
600
800
1000
-90
-60
-30
0
30
60
90
0.08
0.06
0.04
0.02
0.01
0.005
-0.005
-0.01
-0.02
-0.04
-0.06
-0.08

Fig. S5. Global zonally integrated mean annual atmospheric vertical velocity (Pa/s) for each simulation for the pre-industrial 280 ppm (left column), Changhsingian ~252 Ma at 412 ppm, 857 ppm, 1712 ppm, and 2568 ppm (middle column), and Induan ~251 Ma at 879 ppm and 4000 ppm (right column) pCO_2. Negative values indicate vertical ascent, positive values indicate vertical descent.

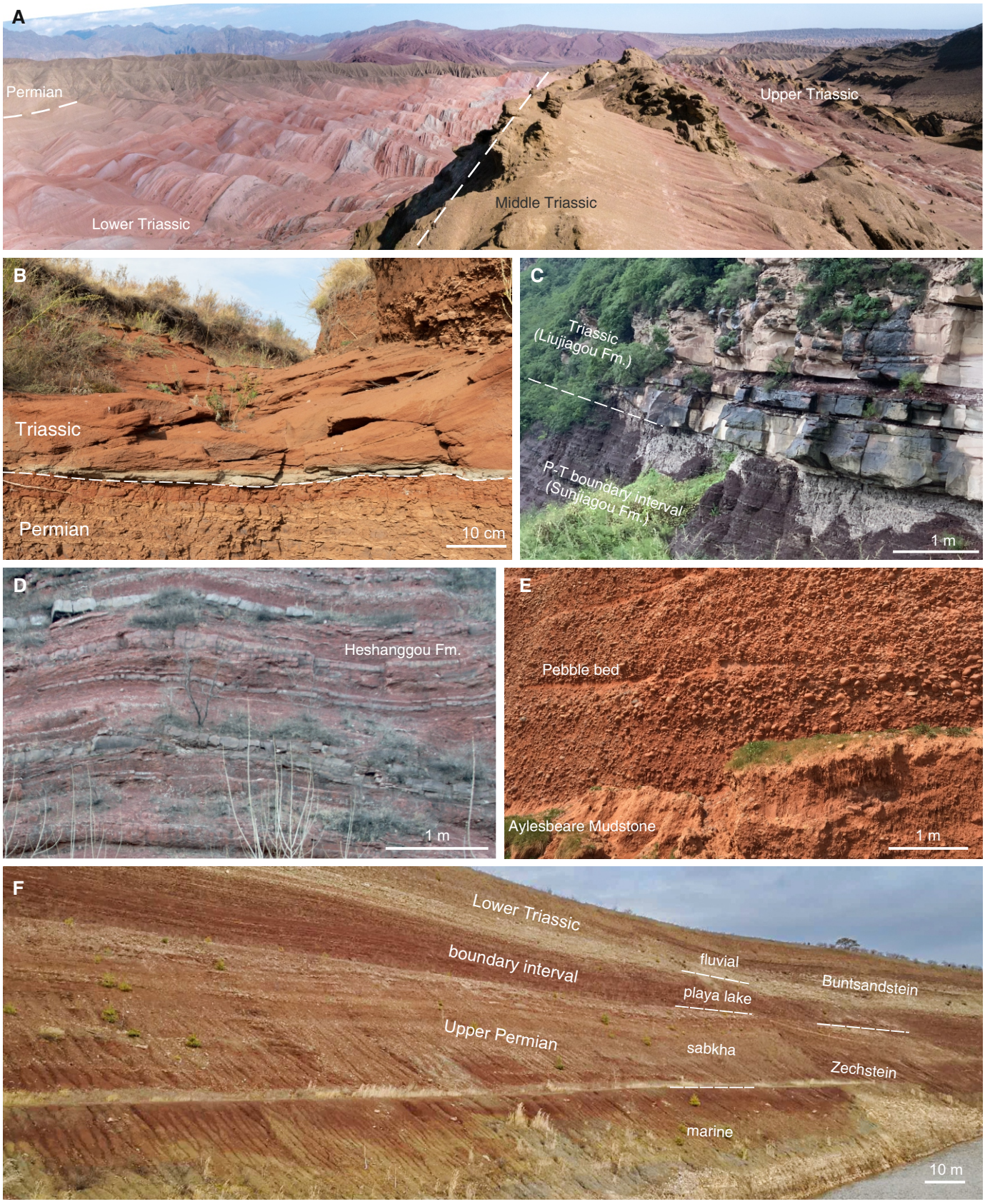
A
Permian
Upper Triassic
Middle Triassic
Lower Triassic
B
Triassic
Permian
10 cm
C
Triassic
(Liujiagou Fm.)
P-T boundary interval
(Sunjiagou Fm.)
1 m
D
Heshanggou Fm.
1 m
E
Pebble bed
Aylesbeare Mudstone
1 m
F
Lower Triassic
boundary interval
Upper Permian
fluvial
playa lake
sabkha
marine
Buntsandstein
Zechstein
10 m

Fig. S6. Field photographs of Upper Permian and Early Triassic terrestrial facies. (A) Panoramic view of the Taodonggou section, showing the transition from plant-bearing late Permian fluvial and deltaic sandstones (far left, light greenish brown in color) to Early Triassic fluvial red beds in the Turpan-Kumul Basin, Xinjiang, northwest China (*105*); (B) The P-T boundary at Boyevaya Gora, Orenburg, Russia. Upper Permian deposits consist of partly bioturbated, planar laminated, brownish to reddish mudstones with white, calcareous concretions recording deposition in low-energy settings, such as floodplains and lakes (c.f. *106*). The overlying Lower Triassic consists of sandstones and pebbly sandstones featuring large-scale trough cross-bedding, recording dune-scale bedforms formed in a fluvial setting. The P-T boundary, with a sharp and erosive contact, is constrained via magnetostratigraphy and biostratigraphy (*107*), but time lost in the hiatus is minor according to magnetostratigraphy (*108*). (C) The P-T boundary beds at Shichuanhe, North China, show the change in fluvial style at the Sunjiagou-Liujiagou formational transition. (D) Sheet flood sandstones from the Heshanggou Formation (overlies the Liujiagou Formation, Olenekian in age) at Dayulin, Henan, North China (photograph courtesy of K.X. Ji), showing continuous interbeds of reddish fine- to medium-grained sandstones commonly displaying planar laminations, and greyish massive mudstone deposits. Planar laminated sandstones record upper flow regime conditions associated with the deposition of sheet flood elements. In contrast, the massive mudstones indicate low-energy subaqueous depositional conditions (e.g., playa lake). The sequence collectively reflects the interaction of distal-fan-derived sheet-flood elements within playa lake settings. (E) Budleigh Salterton Pebble Beds, south Devon, UK, late Spathian. Moderately sorted red conglomerates and pebbly sandstones consisting of sub-rounded to rounded granule to pebble-sized clasts. Large-scale trough-cross bedding and commonly imbricated gravel-size clasts are indicative of high energy, bed-load dominated fluvial transport; (F) P-T transition at the Caaschwitz quarry, Central European Basin, Germany (photograph courtesy of Fabian Käsbohrer). Across the P-T boundary, an over 10-meter-thick wavy to lenticular-laminated brownish claystone and siltstone and fine-sandstone interval, deposited in a sabkha environment, transitions into fine to coarse-grained sandstones associated with the deposition of fluvial channel systems (*109, 110*).

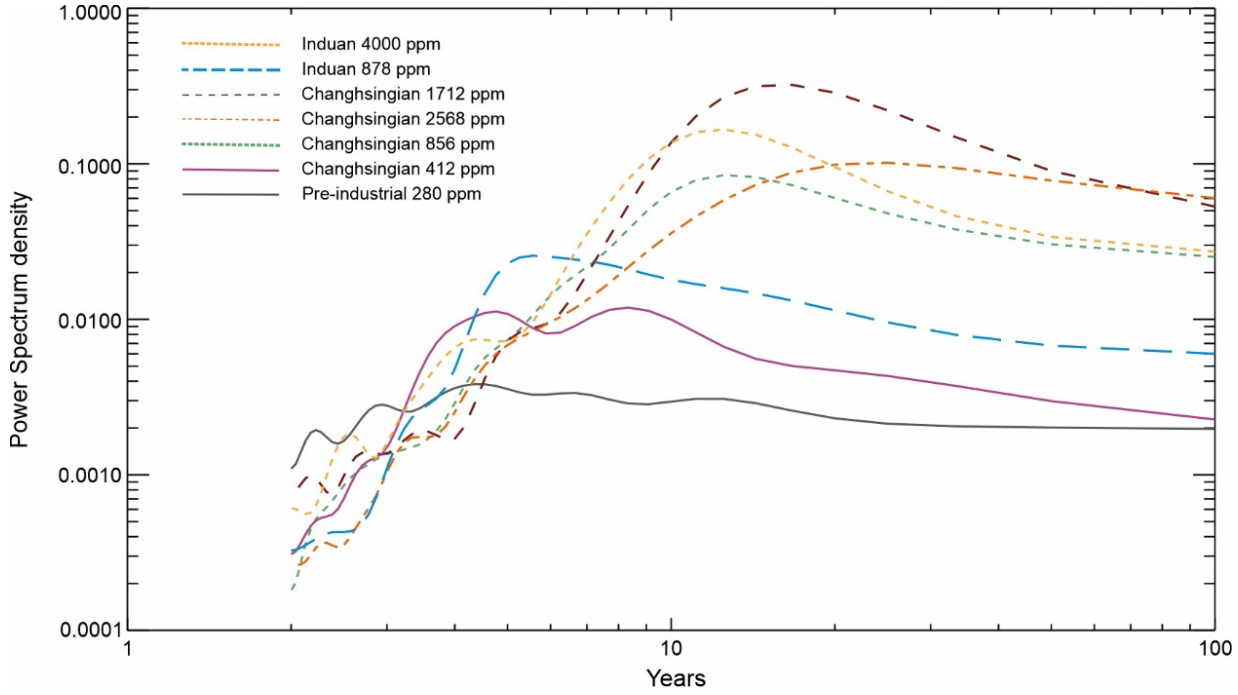

Fig. S7. Mean annual equatorial sea surface temperature power spectral density for the Niño 3.4 equivalent index (see Methods) for each simulation for the pre-industrial period at 280 ppm, Changhsingian ~252 Ma at 412 ppm, 857 ppm, 1712 ppm, and 2568 ppm, and Induan ~251 Ma at 879 ppm and 4000 ppm pCO_2, depicting El Niño periodicity.

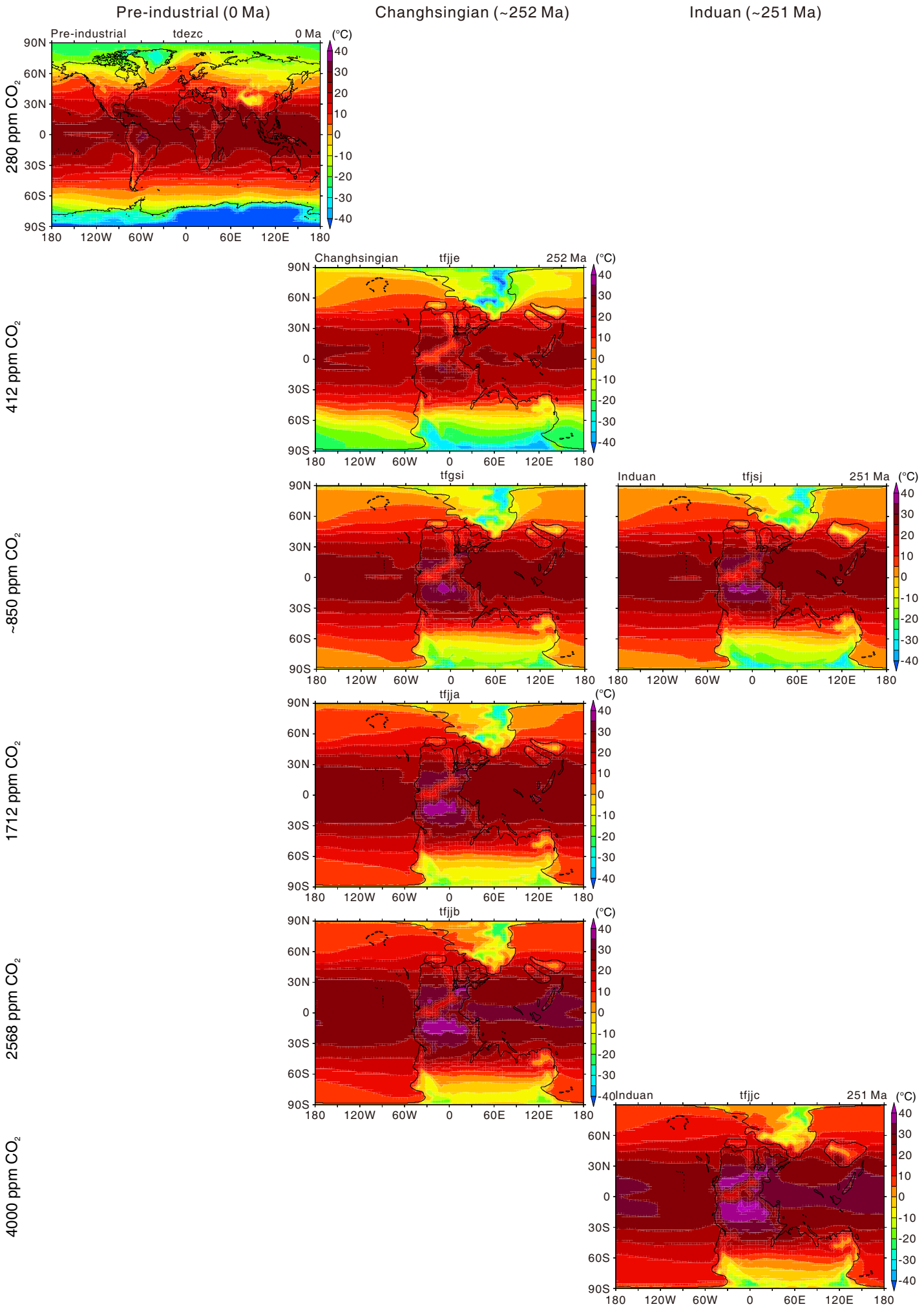
Pre-industrial (0 Ma)
Changhsingian (~252 Ma)
Induan (~251 Ma)
280 ppm CO2
412 ppm CO2
~850 ppm CO2
1712 ppm CO2
2568 ppm CO2
4000 ppm CO2
Pre-industrial tdezc 0 Ma
Changhsingian tfjje 252 Ma
tfgsi
Induan tfjsj 251 Ma
tfjja
tfjjb
Induan tfjjc 251 Ma
(°C)
90N
60N
30N
0
30S
60S
90S
180 120W 60W 0 60E 120E 180
40 30 20 10 0 -10 -20 -30 -40

Fig. S8. Air temperature at 1.5 m height (°C) for each simulation for the pre-industrial period at 280 ppm (left column), Changhsingian ~252 Ma at 412 ppm, 857 ppm, 1712 ppm, and 2568 ppm (middle column), and Induan ~251 Ma at 879 ppm and 4000 ppm (right column) pCO_2.

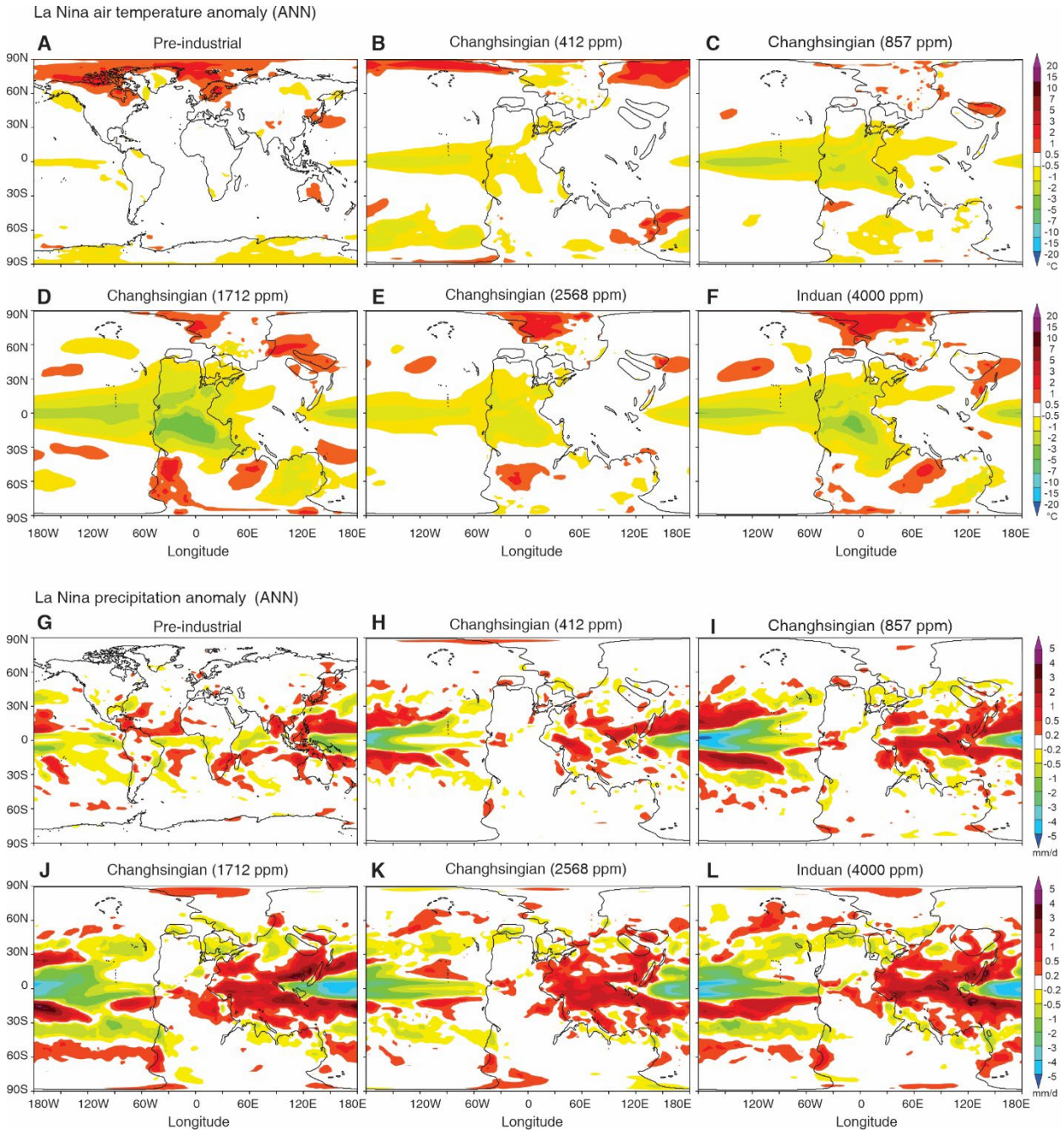

Fig. S9. Composite analysis of five consecutive La Nina. Annual mean 1.5 m air temperature (A-F) and annual mean precipitation (G-L) anomalies during La Nina years, relative to the 100-year climate mean for each time period and pCO_2, in the pre-industrial world and the transition from the pre-crisis (412 ppm) to the peak (4000 ppm) of the P-T crisis world.

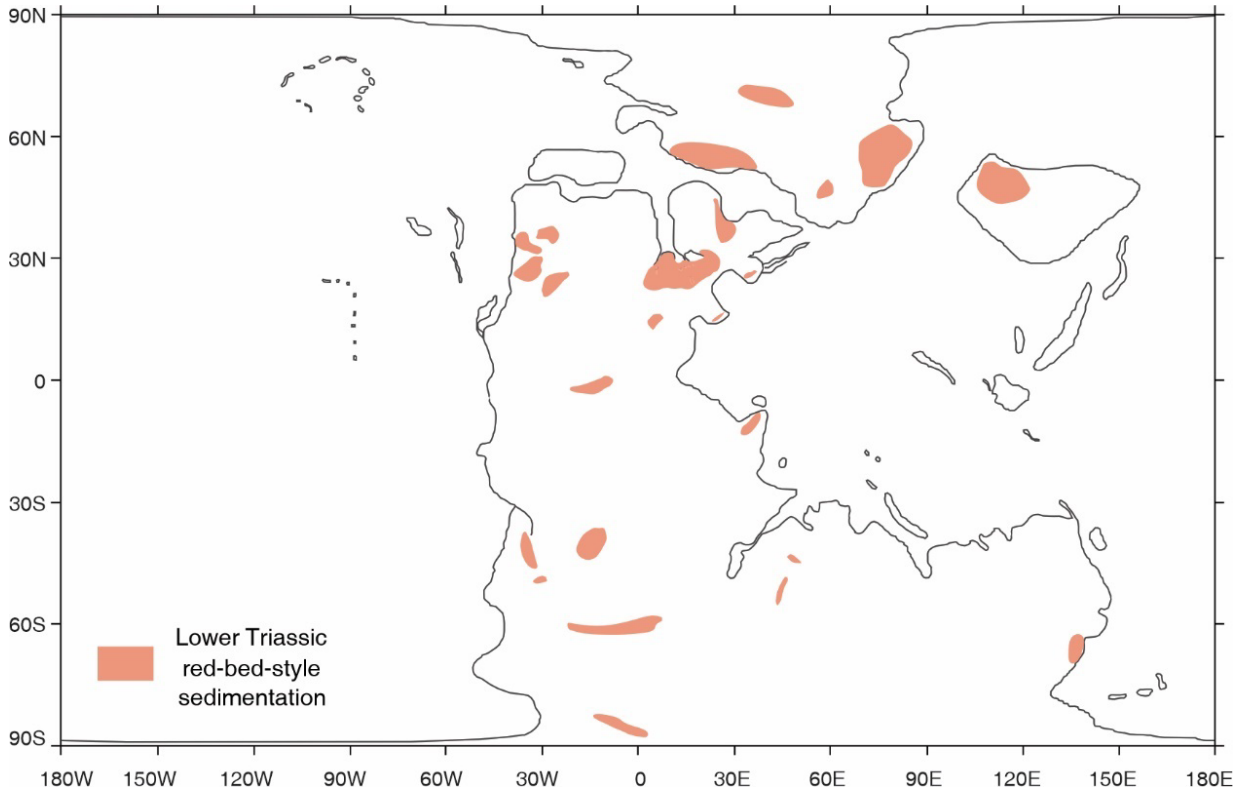

Fig. S10. Distribution of Pangea basins with well-known Permian-Triassic terrestrial red-bed-style sedimentation, showing their extended distribution from ~70 °N to ~80 °S latitude. Data are extracted from published papers [globe summary (*111*), Europe (*85, 112*), Argentina (*113*), Brazil-Uruguay (*32*), Antarctica (*114*), Australia (*79*), North China (*91, 115*), South China (*116*), Jordan (*117*), India (*94*), Morocco (*118*), Russia (*88, 89*), South Africa (*31, 119*) and USA (*120*)]. Note that red bed is an arbitrary term that typically refers to fluvial facies produced by irregular runoff and flashy discharge. However, in literature, the term groups a range of terrestrial rocks and can be highly diachronous in different basins (*100*).

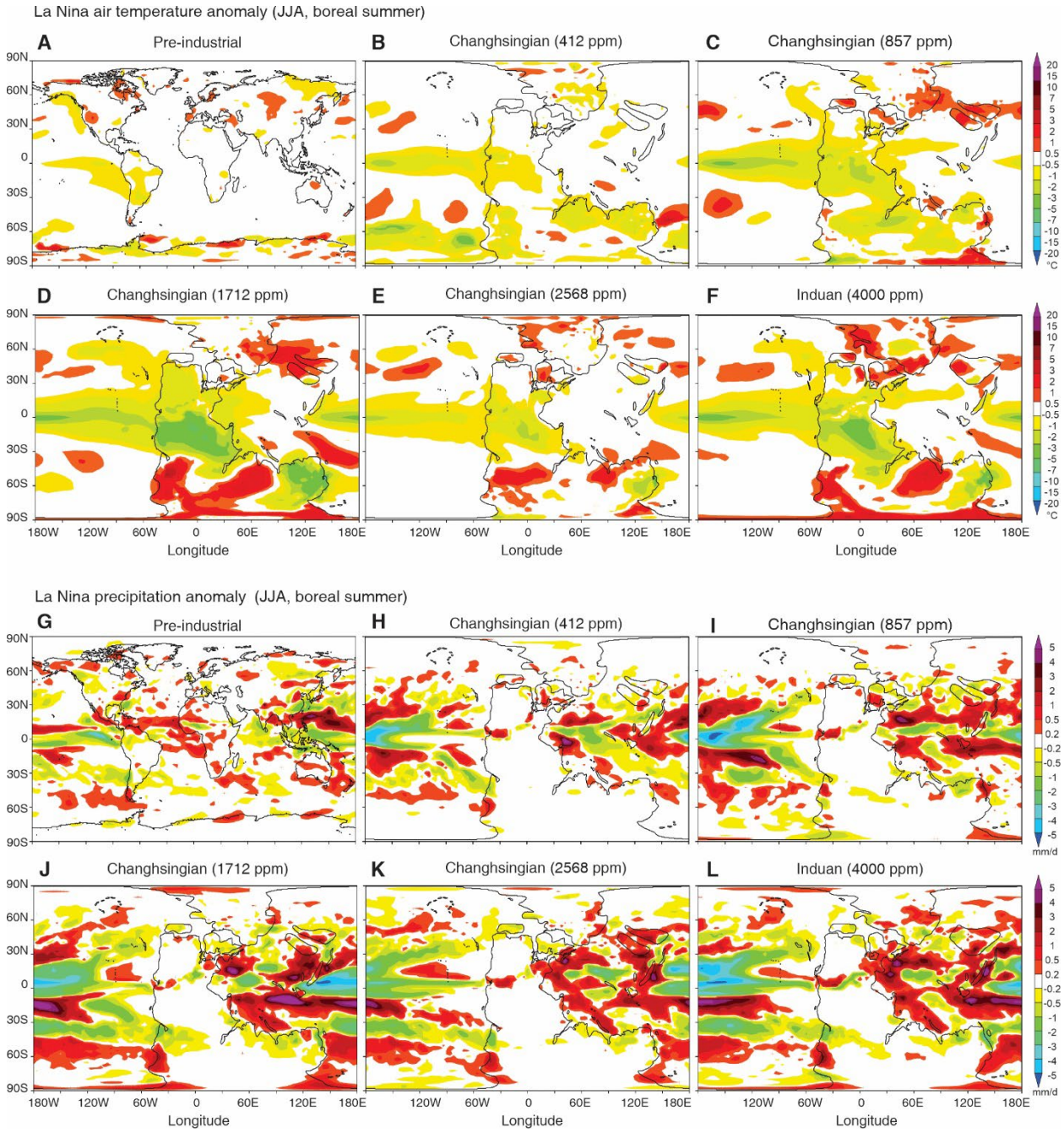

Fig. S11. Composite analysis of boreal summers (JJA) in five consecutive La Nina. JJA 1.5 m air temperature (A-F) and JJA precipitation (G-L) anomalies during La Nina years, relative to the 100-year climate mean for each time period and pCO_2, in the pre-industrial world and the transition from the pre-crisis (412 ppm) to the peak (4000 ppm) of the P-T crisis world.

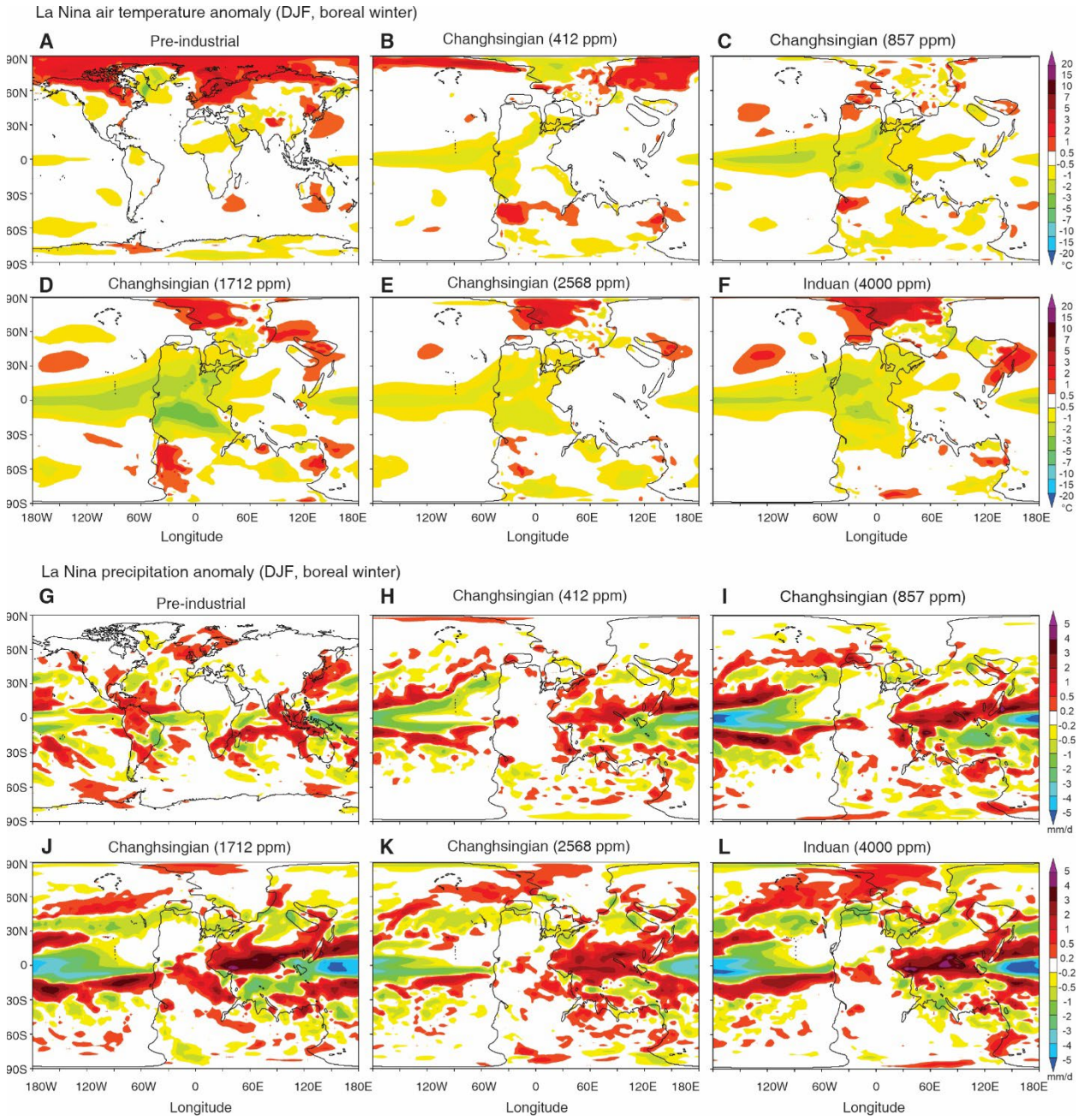

Fig. S12. Composite analysis of boreal winters (DJF) in five consecutive La Nina. DJF 1.5 m air temperature (A-F) and DJF precipitation (G-L) anomalies during La Nina years, relative to the 100-year climate mean for each time period and pCO_2, in the pre-industrial world and the transition from the pre-crisis (412 ppm) to the peak (4000 ppm) of the P-T crisis world.

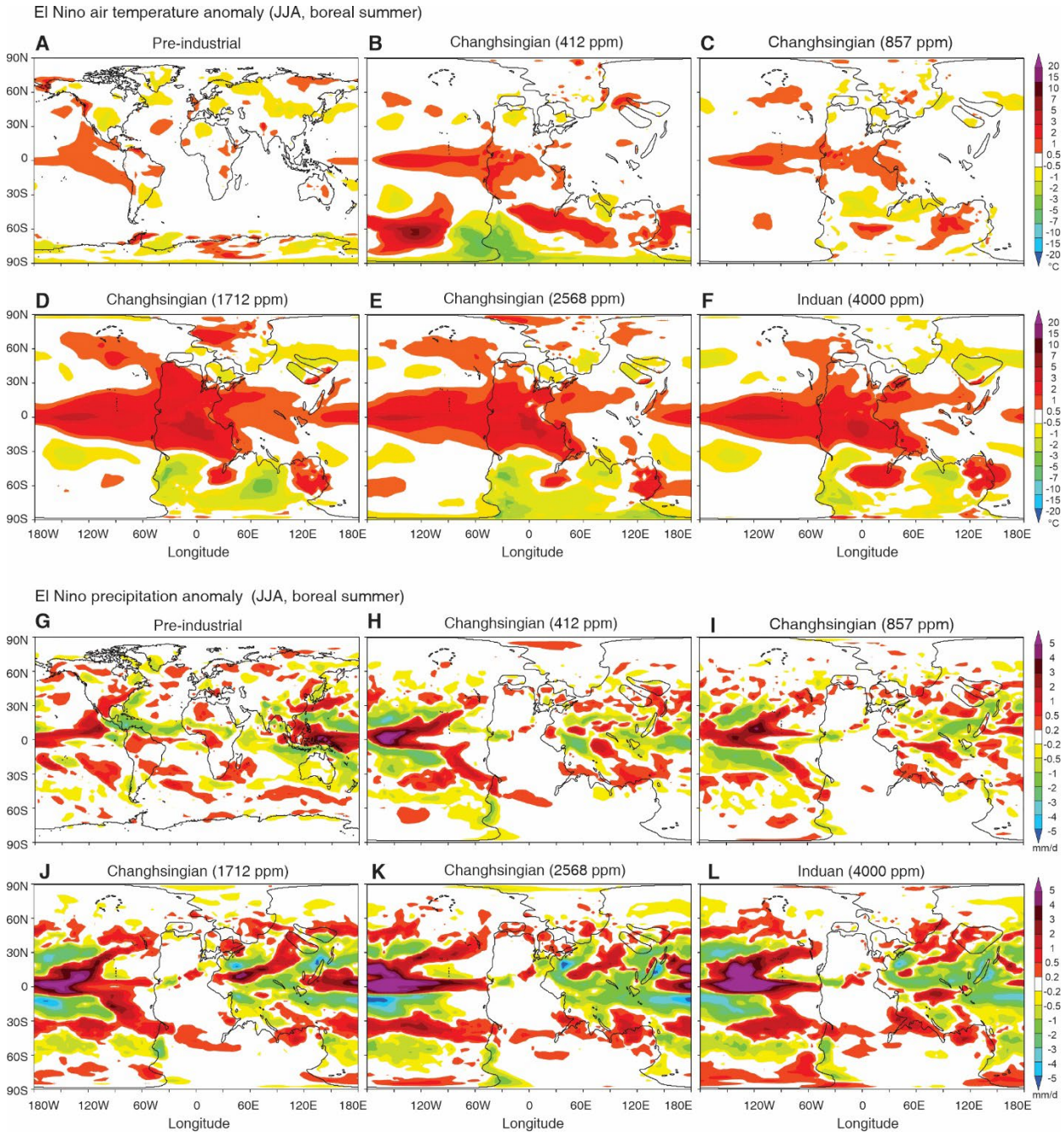

Fig. S13. Composite analysis of boreal summers (JJA) in five consecutive El Niños. JJA 1.5 m air temperature (A-F) and JJA precipitation (G-L) anomalies during El Niños years, relative to the 100-year climate mean for each time period and pCO_2, in the pre-industrial world and the transition from the pre-crisis (412 ppm) to the peak (4000 ppm) of the P-T crisis world.

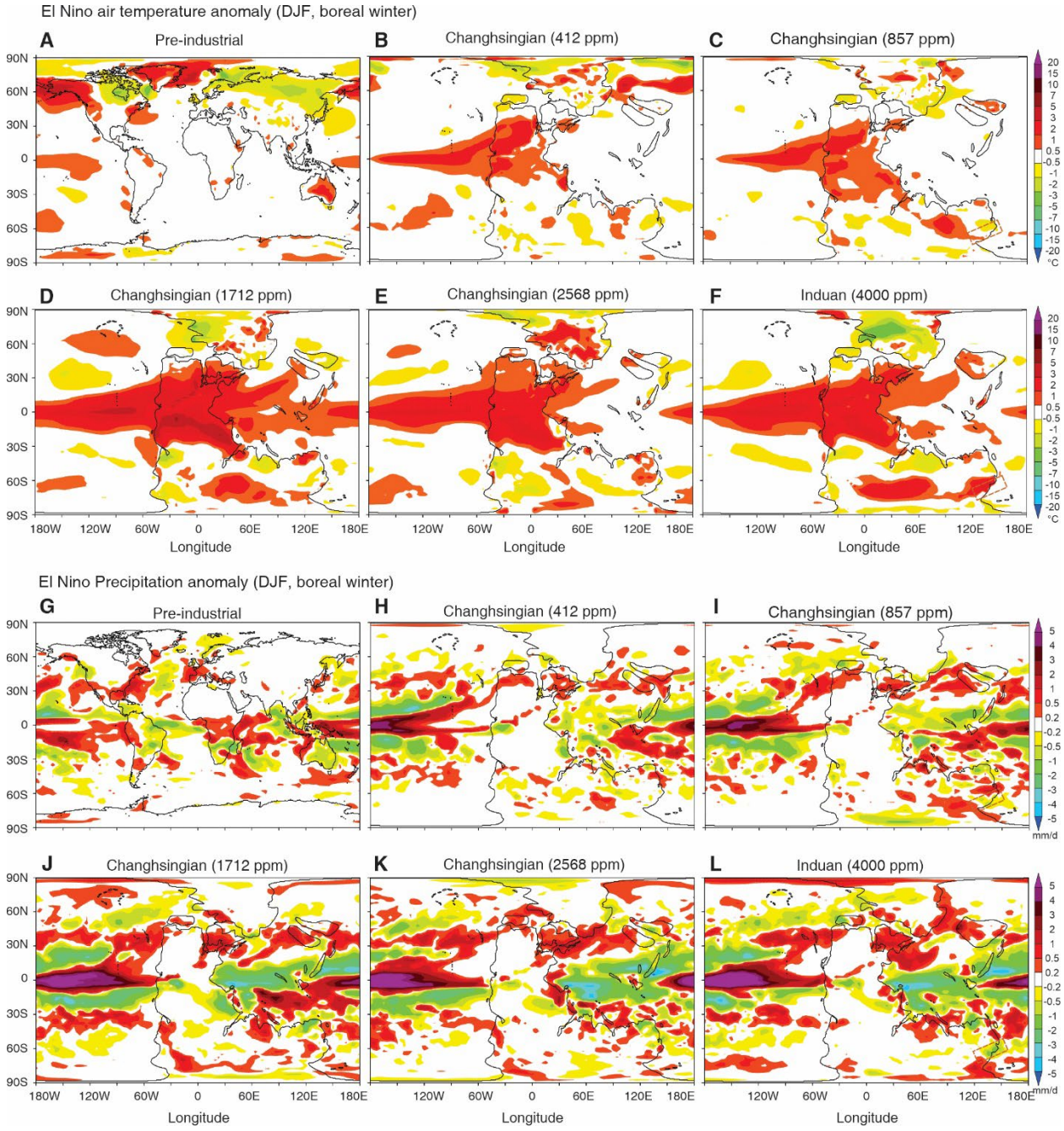

Fig. S14. Composite analysis of boreal winters (DJF) in five consecutive El Niños. DJF 1.5 m air temperature (A-F) and DJF precipitation (G-L) anomalies during El Niños years, relative to the 100-year climate mean for each time period and pCO_2, in the pre-industrial world and the transition from the pre-crisis (412 ppm) to the peak (4000 ppm) of the P-T crisis world. The dashed rectangle indicates the Sydney Basin where the early disappearance of gymnosperm forests is reported (*8*). The region was subject to summer droughts during El Niño years

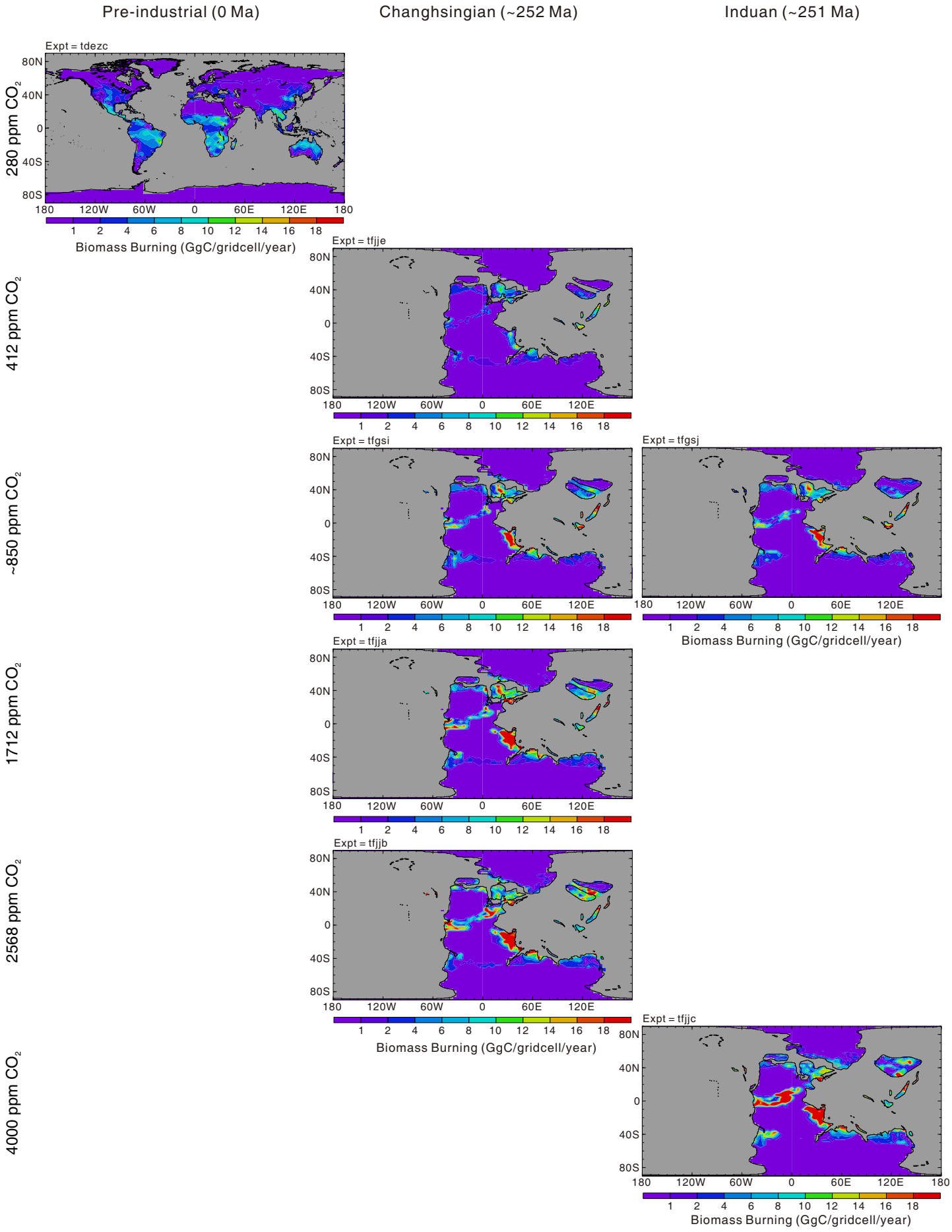
Pre-industrial (0 Ma)
Changhsingian (~252 Ma)
Induan (~251 Ma)
280 ppm CO2
412 ppm CO2
~850 ppm CO2
1712 ppm CO2
2568 ppm CO2
4000 ppm CO2
Expt = tdezc
Expt = tfjje
Expt = tfgsi
Expt = tfgsj
Expt = tfjja
Expt = tfjjb
Expt = tfjjc
80N
40N
0
40S
80S
180
120W
60W
0
60E
120E
1 2 4 6 8 10 12 14 16 18
Biomass Burning (GgC/gridcell/year)

Fig. S15. Simulated biomass burning (Gg/C/yr) using the Sheffield Dynamic Global Vegetation Model for each simulation for the pre-industrial period at 280 ppm (left column), Changhsingian ~252 Ma at 412 ppm, 857 ppm, 1712 ppm, and 2568 ppm (middle column), and Induan ~251 Ma at 879 ppm and 4000 ppm (right column) pCO_2. Key changes include a progressive increase in biomass burning with increasing pCO_2.

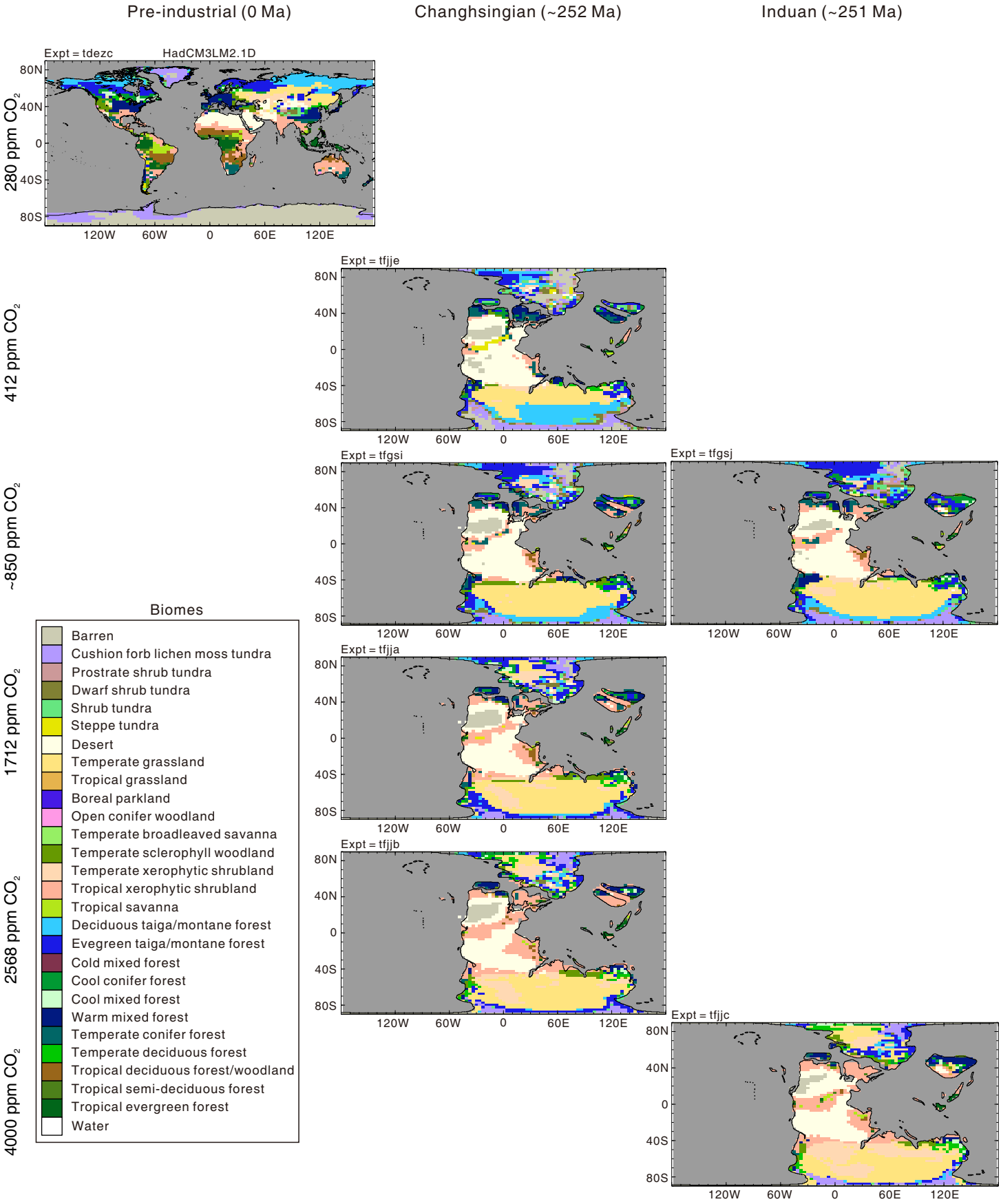
Pre-industrial (0 Ma)
Changhsingian (~252 Ma)
Induan (~251 Ma)
Expt = tdezc
HadCM3LM2.1D
280 ppm CO2
412 ppm CO2
~850 ppm CO2
1712 ppm CO2
2568 ppm CO2
4000 ppm CO2
80N
40N
0
40S
80S
120W
60W
0
60E
120E
Expt = tfjje
Expt = tfgsi
Expt = tfgsj
Expt = tfjja
Expt = tfjjb
Expt = tfjjc
Biomes
Barren
Cushion forb lichen moss tundra
Prostrate shrub tundra
Dwarf shrub tundra
Shrub tundra
Steppe tundra
Desert
Temperate grassland
Tropical grassland
Boreal parkland
Open conifer woodland
Temperate broadleaved savanna
Temperate sclerophyll woodland
Temperate xerophytic shrubland
Tropical xerophytic shrubland
Tropical savanna
Deciduous taiga/montane forest
Evegreen taiga/montane forest
Cold mixed forest
Cool conifer forest
Cool mixed forest
Warm mixed forest
Temperate conifer forest
Temperate deciduous forest
Tropical deciduous forest/woodland
Tropical semi-deciduous forest
Tropical evergreen forest
Water

Fig. S16. Simulated biomes using BIOME4 vegetation model for each simulation for the pre-industrial period at 280 ppm (left column), Changhsingian ~252 Ma at 412 ppm, 857 ppm, 1712 ppm and 2568 ppm (middle column), and Induan ~251 Ma at 879 ppm and 4000 ppm (right column) pCO_2. Key changes in the P-T time include a sharp decrease in deciduous taiga/montane forest (estimated ~21×10^6 km^2 loss in ~25 kyr) in southern Gondwana land when pCO_2 increases from 412 ppm to 857 ppm. Deforestation in North China and in tropical regions occurred after southern deforestation.

Pre-industrial (0 Ma)

Changhsingian (~252 Ma)

Induan (~251 Ma)

280 ppm CO_2

412 ppm CO_2

~850 ppm CO_2

1712 ppm CO_2

2568 ppm CO_2

4000 ppm CO_2

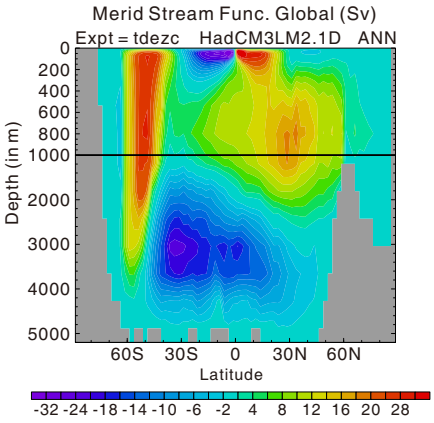

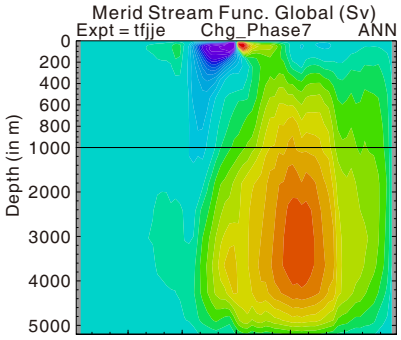

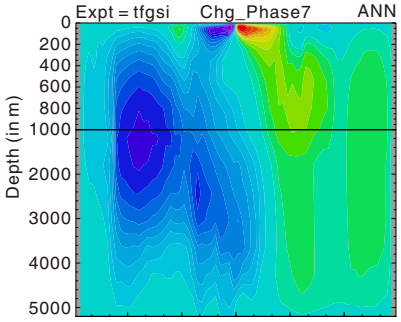

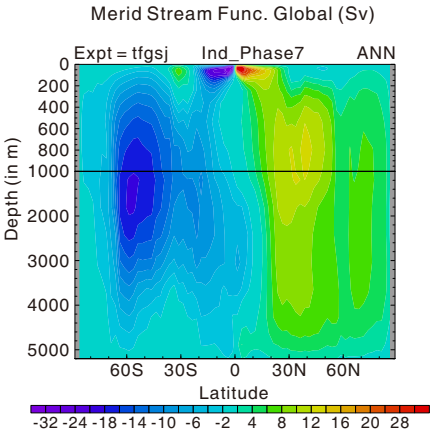

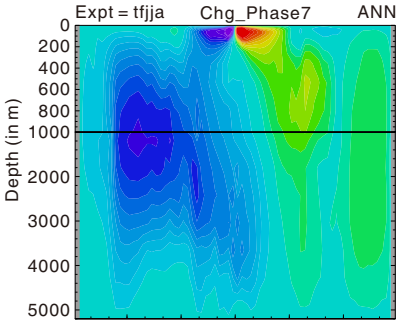

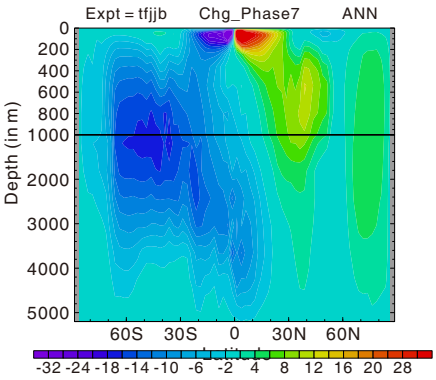

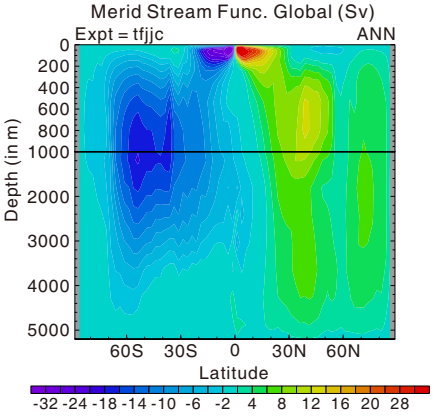

Fig. S17. Zonally-integrated mean annual meridional overturning circulation (MOC) stream function (Sv) for each simulation for pre-industrial period at 280 ppm (left column), Changhsingian ~252 Ma at 412 ppm, 857 ppm, 1712 ppm, and 2568 ppm (middle column), and Induan ~251 Ma at 879 ppm and 4000 ppm (right column) pCO_2. Key changes are a reorganization and weakening of global ocean circulation with increasing pCO_2, especially from 412 ppm to 857 ppm.

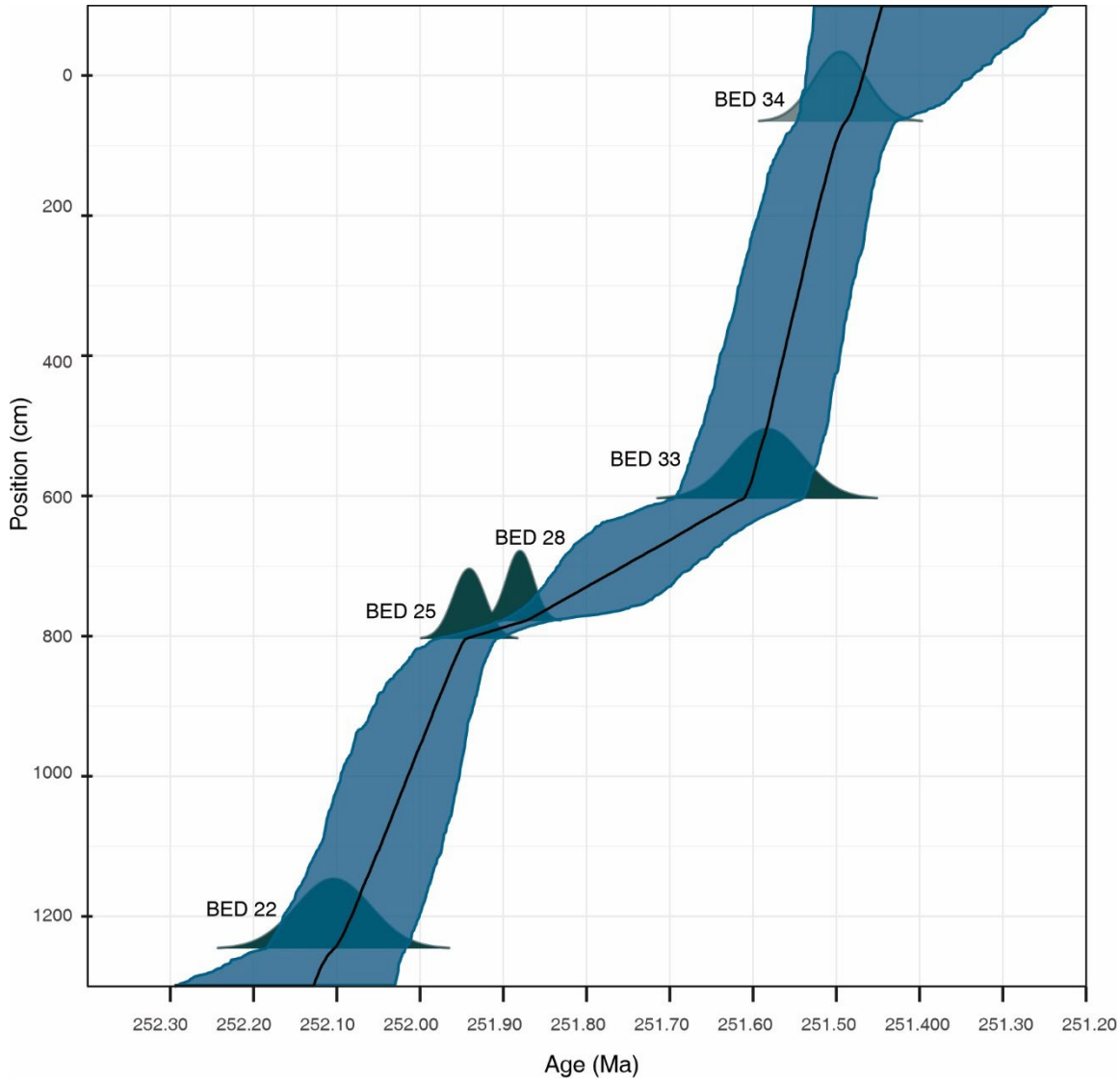

Fig. S18 Bayesian age model for the Permian-Triassic beds at Meishan, South China. U-Pb age constraints and R-coding for establishing the age-depth model are from (*48*) and (*59*), respectively. Depths are adapted from (*60*) by assigning the top of Bed 34 as 0 cm. Positions on the Y axis indicate depth below the top of Bed 34.

Table S1. Sampling site information and oxygen isotope values of late Smithian conodonts from different geographic settings.

Sample ID.	Conodonts	Age assignment	$\delta^{18}O_{PO4}$	reproducibility	Estimated temperature
			‰	1 σ	°C, $\delta^{18}O_{sw}$=-1‰
		Eastern Pangea Margin (Western Tetheys)			
		Werfen Fm., Vigil section, Southern Tyrol, Italy CAI=2, Sampled by L.Krystyn,			
		GPS: 46°41'09.5" N; 11°55'40.6" E.			
RS 156	*Foliella gardenae*	late to latest Smithian	16.4	0.06	41.5
	Pachycladina	late to latest Smithian	16.5	0.03	41.1
		Muć, Werfen Formation, Croatia, CAI=4. Sampled by L.Krystyn			
		GPS: 43°41'24.10"N, 16°32'10.93"E.			
ZC-23	*Pachycladina, Foliella gardenae*	late Smithian	16.7	0.14	40.2
		Western Laurentia Margin			
		Georgetown, ID, USA, CAI=3, sampled by M.J.Orchard			
		GPS: 42°28'45.6" N, 111° 24'44.6" W.			
93-OF-W-8	*Scythogondolella*	Tardus Zone, late Smithian	16.9	0.06	39.4
		Southwestern Gondwana Margin (Neotetheys)			
		Exotic block, Ibra, Oman, CAI=1, sampled by L.Krystyn			
		GPS: 22°44'45.8" N; 58°38'12.2" E.			
01/93	*Neospathodus*	late Smithian	16.3	0.10	41.9
		Eastern Tethys			
		Laren, South China, CAI=4-5, sampled by Y.D.Sun			
		GPS: 24° 36' 26.32" N, 106° 52' 39" E.			
LRC 06	*Pachycladina*	late Smithian	16.8	0.20	39.8

Table S2. Age assignments and duration of P-T conodont zones at the Meishan D GSSP section, using a Bayesian age model based on U-Pb ages of Burgess et al (*48*).

Conodont zones‡	Thickness /cm	Beds	Depth /cm	Age/ Ma	1sd /Ma	Duration/kyr	1sd /ka
*I. isarcica**	777	29-51	0	251.474	0.036	398	39
			777	251.872	0.015		
I. staeschei	7	27d-28	777	251.872	0.015	17	20
			784	251.889	0.013		
H. parvus	4	27c	784	251.889	0.013	11	18
			788	251.900	0.013		
H. changxingensis	8	27a-b	788	251.900	0.013	23	19
			796	251.923	0.014		
C. meishanensis	10	25-26	796	251.923	0.014	24	23
			806	251.947	0.018		
C. yini	286	23-24	806	251.947	0.018	107	39
			1092	252.054	0.035		

‡ Using the conodont zonation of Jiang et al. (*121*).

* Age and thickness calculated to the top of Bed 34.

Table S3. Age assignments and duration of P-T beds at the Meishan D GSSP section, using a Bayesian age model based on U-Pb ages of Burgess et al. (*48*).

Bed No.	thickness/	Height/cm	comment	Depth/cm	Age/ Ma	1sd (Ma)	Duration/Myr	1sd (Ma)
34	600	5000	top	0	251.474	0.036	0.138	0.053
		4934	ash layer	66	251.495	0.032		
		4400	base	600	251.612	0.039		
33	8	4400	top	600	251.612	0.039	0.008	0.056
		4396	ash layer	604	251.583	0.043		
		4392	base	608	251.620	0.040		
32	82	4392	top	608	251.620	0.040	0.127	0.051
		4310	base	690	251.747	0.031		
31	4	4310	top	690	251.747	0.031	0.005	0.043
		4306	base	694	251.752	0.030		
30	57	4306	top	694	251.752	0.030	0.082	0.034
		4249	base	751	251.834	0.017		
29	26	4249	top	751	251.834	0.017	0.038	0.023
		4223	base	777	251.872	0.015		
28	3	4223	top	777	251.872	0.015	0.006	0.021
		4221.5	ash layer	778.5	251.880	0.016		
		4220	base	780	251.878	0.014		
27	16	4220	top	780	251.878	0.014	0.045	0.020
		4204	base	796	251.923	0.014		
26	6	4204	top	796	251.923	0.014	0.016	0.022
		4198	base	802	251.939	0.017		
25	4	4198	top	802	251.939	0.017	0.008	0.025
		4196	ash layer	804	251.941	0.019		
		4194	base	806	251.947	0.018		
24	88	4194	top	806	251.947	0.018	0.040	0.030
		4106	base	894	251.987	0.024		
24e	30	4194	top	806	251.947	0.018	0.016	0.028
		4164	base	836	251.963	0.021		
24d	22	4164	top	836	251.963	0.021	0.009	0.030
		4142	base	858	251.972	0.021		
24c	17	4142	top	858	251.972	0.021	0.007	0.030
		4125	base	875	251.979	0.022		
24b	10	4125	top	875	251.979	0.022	0.004	0.032
		4115	base	885	251.983	0.023		
24a	9	4115	top	885	251.983	0.023	0.004	0.033
		4106	base	894	251.987	0.024		
23	123	4106	top	894	251.987	0.024	0.045	0.042
		3983	base	1017	252.032	0.034		
22	219	3983	top	1017	252.032	0.034	0.068	0.053
		3764	base	1236	252.100	0.041		
21	112	3764	top	1236	252.100	0.041	0.031	0.071
		3754	layer "Bed	1246	252.104	0.045		
		3652	base	1348	252.131	0.058		

Table S4. Oxygen isotope values from conodont bioapatite from the Upper Permian (Changhsingian) to the Middle Triassic (Anisian) and calculated SST gradient across the equatorial Tethys.

Age/Ma	$\delta^{18}O$ /‰ VSMW West Tethys	$\delta^{18}O$/‰ VSMW East Tethys	$\delta^{18}O$/‰ VSMW western Laurentia	Δ18O/‰	Δtemp/°C
244.500	18.6	18.5		0.1	0.4
246.750	17.6	18.5		0.9	3.8
247.580	17.5	17.7		0.2	0.8
247.705	16.9	17.7		0.8	3.4
247.800	16.7	17.6		0.9	3.8
248.065		18.4	19.2	0.8	3.4
248.185	17.0	18.0		1.0	4.2
248.335	17.3	18.1		0.8	3.4
248.565	17.4	18.2		0.8	3.4
248.735	17.6	18.1		0.5	2.1
249.085	16.4	16.8		0.4	1.7
249.205	16.5	16.8	16.9	0.4	1.7
249.280	16.1	16.9		0.8	3.4
249.295	16.7	16.9		0.2	0.8
249.335	16.0	16.9		0.9	3.8
249.780	18.6	18.3		-0.3	1.3
249.815	18.0	18.5		0.5	2.1
249.880	17.9	18.6		0.7	2.9
250.150	17.2	18.1		0.9	3.8
250.250	17.1	18.1		1.0	4.2
250.400	17.3	18.0		0.7	2.9
250.480	17.2	18.0		0.8	3.4
250.550	17.4	17.9		0.5	2.1
250.690	16.9	17.9		1.0	4.2
250.730	17.0	17.9		0.9	3.8
250.870	17.4	17.9		0.5	2.1
251.230	17.2	17.4		0.2	0.8
251.850	17.6				
251.853		17.9			
251.855	18.5				
251.860	17.3				
251.865	18.0				
251.871	17.7				
251.873		18.4			
251.876	17.9				
251.884	17.6	18.5		0.9	3.8
251.895	17.8	18.5		0.7	2.9
251.906	17.5	18.6		1.1	4.6

251.914	17.6			
251.917		18.5		
251.920	18.1			
251.925	18.6			
251.931		20.1		
251.935	19.4			
251.945	19.9			
251.947		20.0		
251.951		20.4		
251.955	19.5	20.4	0.9	3.8
251.958		20.3		
251.960	19.6			
251.961		20.1		
251.963	20.0			
251.964		19.9		
251.966		20.5		
251.968	20.2	20.5	0.3	1.3
251.970		20.7		
251.971	19.8			
251.972		20.1		
251.973		20.3		
251.975		20.3		
251.976	19.4			
251.977		20.1		
251.979		19.8		
251.980	19.5			
251.981		19.7		
251.983		20.1		
251.984	20.0			
251.985		20.4		
251.986	19.6			
251.987		20.6		
251.989	18.9			
251.990		21.1		
251.993	19.4			
251.998		21.1		
251.999	19.4			
252.005	19.6			
252.006		21.0		
252.008	20.0			
252.012	19.9			
252.014		21.4		
252.016	18.6			
252.020	19.3			
252.022		21.4		

252.026	19.7			
252.030		20.4		
252.032	19.1			
252.032	19.1	21.4	2.3	9.7
252.033		20.9		
252.038	18.9			
252.040		20.7		
252.043	19.9			
252.044		20.7		
252.050	19.4			
252.050	19.4	20.3	0.9	3.8
252.060	19.4			
252.067		20.4		
252.068	19.2			
252.068	19.2	21.0	1.8	7.6
252.120		21.0		
252.180	19.2	20.3	1.1	4.6
252.265	19.6	20.7	1.1	4.6
252.410	19.5	21.0	1.5	6.3
252.550	19.2	21.4	2.2	9.2
252.950	19.7	20.7	1.0	4.2
252.970	19.2	20.7	1.5	6.3
252.995	19.0	21.1	2.1	8.8
253.020	18.9	20.4	1.5	6.3
253.230	19.0	20.0	1.0	4.2
253.265	18.9	21.2	2.3	9.7
253.305	19.4	20.6	1.2	5.0
253.620	19.5	20.0	0.5	2.1
253.680	18.9	19.7	0.8	3.4
253.820	19.4	20.7	1.3	5.5

The end of Table S4.

Table S5. Calculated high-resolution zonal SST gradient across the P-T transition using generalized additive models.

Age/Ma	eastern Tethys SST /°C	western Tethys SST/°C	Δ SST /°C
251.840	37.0	35.0	-2.0
251.845	36.2	35.1	-1.1
251.850	35.5	35.2	-0.3
251.855	34.8	35.4	0.5
251.860	34.1	35.5	1.4
251.865	33.5	35.6	2.1
251.870	33.1	35.8	2.7
251.875	32.9	35.9	3.1
251.880	32.8	36.1	3.3
251.885	32.8	36.2	3.4
251.890	32.7	36.2	3.5
251.895	32.5	36.1	3.7
251.900	32.2	36.0	3.8
251.905	32.2	35.6	3.5
251.910	32.6	35.1	2.5
251.915	32.7	34.4	1.7
251.920	31.4	33.5	2.1
251.925	28.9	32.4	3.5
251.930	26.5	31.3	4.8
251.935	25.4	30.2	4.8
251.940	25.4	29.3	3.9
251.945	25.6	28.6	2.9
251.950	25.3	28.0	2.7
251.955	25.0	27.6	2.6
251.960	25.4	27.3	1.9
251.965	25.3	27.3	2.0
251.970	24.5	27.3	2.9
251.975	25.5	27.5	2.0
251.980	26.9	27.7	0.8
251.985	25.0	28.0	3.0
251.990	22.0	28.2	6.2
251.995	21.2	28.3	7.1
252.000	21.8	28.4	6.6
252.005	22.1	28.5	6.4
252.010	21.1	28.6	7.4
252.015	20.2	28.7	8.5
252.020	20.6	28.9	8.3
252.025	21.9	28.9	7.1
252.030	23.2	29.0	5.8
252.032	20.4*	30.1*	9.7*
252.035	23.6	29.0	5.4

252.040	23.4	29.0	5.6
252.045	23.2	29.0	5.8
252.050	23.3	29.0	5.7
252.055	23.6	29.0	5.4
252.060	24.0	29.1	5.0
252.065	24.5	29.2	4.7
252.070	24.8	29.3	4.5

*Values form direct $\delta^{18}O$ measurements (for comparison purposes).

The end of Table S5.

Modeling data availability statement

Model data can be accessed from the repository in netcdf format at www.bridge.bris.ac.uk/resources/simulations.